View metadata, citation and similar papers at core.ac.uk

brought to you by CORE

provided by DSpace@MIT

Differential Cross Section Measurement for the d(n,np) Reaction

by

Sho Uemura

Submitted to the Department of Physics
in partial fulfillment of the requirements for the degree of

Bachelor of Science in Physics

at the

MASSACHUSETTS INSTITUTE OF TECHNOLOGY

June 2010

© Massachusetts Institute of Technology 2010. All rights reserved.

Author . . . .
Department of Physics
May 7, 2010

Certified by . . . .
June L. Matthews
Professor of Physics
Thesis Supervisor

Accepted by . . . .
Professor David E. Pritchard
Senior Thesis Coordinator, Department of Physics

Differential Cross Section Measurement for the d(n,np) Reaction

by

Sho Uemura

Submitted to the Department of Physics
on May 7, 2010, in partial fulfillment of the
requirements for the degree of
Bachelor of Science in Physics

Abstract

The differential cross section for the quasielastic d(n,np) neutron-induced deuteron breakup reaction was measured as a function of incident and scattered particle energies and angles, using a liquid deuterium target at the Weapons Neutron Research (WNR) spallation neutron beam at the Los Alamos Neutron Science Center at the Los Alamos National Laboratory. Cross sections were computed for the incident neutron energy ranges of 100 ± 10, 200 ± 10, and 300 ± 10 MeV. We used proton detectors covering a range of $\theta = 17° - 25°$ in the lab frame, and neutron detectors covering a range of $\theta = 55° - 76°$ in the lab frame. Experiment setup and data analysis are discussed, and preliminary results are presented for the cross section.

Thesis Supervisor: June L. Matthews
Title: Professor of Physics

Acknowledgments

I am grateful to Professor June Matthews for guiding me through this project, all the way from convincing me to take it on through to completing this thesis. Also many thanks to Vlad Henzl, for providing his experience and intuition, and for always having a sound second opinion on analysis and writing. The experiment also could not have succeeded without the support of Art Bridge and Steve Wender at LANL. The ideas of Professors Mark Yuly and Taylan Akdoğan were key to parts of the analysis. Also, thanks to Katrina Koehler, Peter Kroening, Jonathan Slye, and Jared Turkewitz, for being a great team that got the work done. Last but not least, I thank my parents for everything I have achieved.

Contents

1 Introduction **17**

1.1 Quasielastic Scattering 18

2 Experimental Setup **19**

2.1 Neutron Beam Source 19

2.2 Fission Chamber Neutron Beam Monitor 20

2.3 Liquid Deuterium Target 20

2.4 Detector Layout 21

  2.4.1 Neutron Detectors 21

  2.4.2 Proton Detectors 22

  2.4.3 ΔE-E Deuteron Detector 24

  2.4.4 Position Calibration Detectors 24

2.5 Electronics and Data Acquisition 24

  2.5.1 Master Trigger 25

2.6 Experiment Run Periods 27

3 Detector Signal Processing **31**

3.1 ADC Processing and Calibration 31

3.2 TDCs and Time of Flight 32

  3.2.1 TDC Calibration 33

3.3 Time Offsets 33

3.4 Neutron Bar Event Timing and Position 36

  3.4.1 Neutron Height Calibration 37

- 3.5 Wire Chamber Signal Processing 38
  - 3.5.1 Determination of Wire Number 38
  - 3.5.2 Determination of Drift Distance 38
  - 3.5.3 Odd-Even Amplifiers 39
  - 3.5.4 Wire Chamber Position 40
- 3.6 Tracking 41
  - 3.6.1 Coordinate Systems 41
  - 3.6.2 Track Fitting 42

4 Determination of Event Kinematics 47

- 4.1 Determination of Scattered Proton Kinematics by Time of Flight . . 47
- 4.2 Correction for Proton Energy Loss in DE1 48
- 4.3 Determination of Incident and Scattered Neutron Kinematics by Time of Flight 49
- 4.4 Scattering Kinematics 50
  - 4.4.1 Expected Energies and Angles 50

5 Cross-Section Calculation 53

- 5.1 Event Cuts 53
  - 5.1.1 Trigger Cuts 54
  - 5.1.2 Velocity Cuts 54
  - 5.1.3 Scattering Kinematics Cut 55
  - 5.1.4 Proton Track Cut 56
  - 5.1.5 Proton ADC Cut 56
  - 5.1.6 Rear Wire Chamber Cut 56
- 5.2 Background Subtraction 56
- 5.3 Neutron Geometric Acceptance 57
- 5.4 Proton Geometric Acceptance 58
- 5.5 Detector Efficiencies 60
- 5.6 Flux and Target Normalization 62

6 Results **65**

6.1 Error Analysis 65

6.1.1 Time of Flight Energy Resolution 65

6.1.2 Proton Angular Resolution 67

6.1.3 Neutron Angular Resolution 67

6.2 Energy-Dependent Cross Sections 68

6.3 Angle-Dependent Cross Sections 69

7 Conclusions **81**

List of Figures

2-1 Flight paths at the Weapons Neutron Research facility, oriented with the proton beam pointing downwards. 28

2-2 Neutron beam profile, measured with a phosphor image plate placed just upstream of the fission chamber. The actual width of this image is 10.16 cm (4 inches). 29

2-3 Detector layout, as seen from above. 30

3-1 FERA channel numbers with time calibrator input, period 10 ns. . . 34

3-2 $t_{detector} - t_0$ for P1, with gamma flash at approximately 66 ns. 35

3-3 $\frac{1}{2}(tdc_{N,top} + tdc_{N,bot})$ for bar 1. The dips and peaks between -5 and 0 ns suggest that this time difference is not completely linear in position, introducing systematic error. 36

3-4 $\frac{1}{2}(tdc_{N,top} + tdc_{N,bot})$ for bar 1, integrating only events which trigger the first plastic scintillator bar. 37

3-5 Anode time difference for WC1 X1 (run 420 data only). Red lines mark the time differences corresponding to wires, starting with wire 0. . . . 39

3-6 Time sum for WC1 X1, integrated over all liquid deuterium target runs. 40

3-7 Time-to-distance function for WC1 X1. 41

3-8 Drift distances (in cm) for WC1 X1, integrated over all liquid deuterium target runs. 42

3-9 Odd-even amplifier outputs (in units of FERA channels) for WC1 X1 events where the WC1 X1 anode TDCs fired, integrated over all liquid deuterium target runs; the plot on the right is a zoomed version of the plot on the left. The O-E difference (X axis) is offset so that the cutoff between odd and even events is at 0. 43

3-10 O-E difference for WC1 X1 events where the WC1 X1 anode TDCs fired, integrated over all liquid deuterium target runs. 44

3-11 b_x for WC1 tracks, integrated over all liquid deuterium target runs. . 45

4-1 $E_{p,tof}/E_{p,elastic}$ dependence on E_{in}. Note the drop-off due to proton energy loss at low E_{in}. 49

4-2 $E_p/E_{p,elastic}$ dependence on E_{in}, after the energy loss correction. . . . 49

5-1 $E_{n,elastic}$ plotted against E_n. Note the diagonal band of quasielastic scattering events, and the vertical band of background events. 55

5-2 Event counts for neutron bars 1 through 9, plotted with respect to E_n (X axis) and E_p (Y axis), for $E_{in} = 300 \pm 10$ MeV and liquid deuterium target data. 57

5-3 Quadruple differential cross section with respect to θ_p, θ_n, E_p, and E_n in units of mb/MeV^2/sr^2 for $E_{in} = 100 \pm 10$ MeV. 58

5-4 θ_p angles accepted at E_{in} ranges of 100 ± 10 MeV, 200 ± 10 MeV, and 300 ± 10 MeV. 60

5-5 Incident neutron flux integrated over all runs with liquid deuterium target (left) and over all runs with empty target (right). The sharp peak at low energy may be either an artifact of the TDC or a 6.66 MeV resonance in the fission cross section (described in [7]). 62

6-1 Uncertainty σ_E in time-of-flight energy measurement, as a function of energy E. 68

6-2 Quadruple differential cross section with respect to θ_p, θ_n, E_p, and E_n in units of mb/MeV^2/sr^2 for $E_{in} = 100 \pm 10$ MeV. 69

6-3 Quadruple differential cross section with respect to θ_p, θ_n, E_p, and E_n in units of mb/MeV^2/sr^2 for $E_{in} = 200 \pm 10$ MeV. 70
6-4 Quadruple differential cross section with respect to θ_p, θ_n, E_p, and E_n in units of mb/MeV^2/sr^2 for $E_{in} = 300 \pm 10$ MeV. 71
6-5 Triple differential cross section with respect to θ_p, θ_n, and E_p in units of mb/MeV/sr^2 for $E_{in} = 100 \pm 10$ MeV. 72
6-6 Triple differential cross section with respect to θ_p, θ_n, and E_p in units of mb/MeV/sr^2 for $E_{in} = 100 \pm 10$ MeV. 73
6-7 Triple differential cross section with respect to θ_p, θ_n, and E_p in units of mb/MeV/sr^2 for $E_{in} = 100 \pm 10$ MeV. 74
6-8 Triple differential cross section with respect to θ_p, θ_n, and E_n in units of mb/MeV/sr^2 for $E_{in} = 100 \pm 10$ MeV. 75
6-9 Triple differential cross section with respect to θ_p, θ_n, and E_n in units of mb/MeV/sr^2 for $E_{in} = 100 \pm 10$ MeV. 76
6-10 Triple differential cross section with respect to θ_p, θ_n, and E_n in units of mb/MeV/sr^2 for $E_{in} = 100 \pm 10$ MeV. 77
6-11 Double differential cross section with respect to θ_p and θ_n in units of mb/sr^2 for $E_{in} = 100 \pm 10$ MeV. 78
6-12 Double differential cross section with respect to θ_p and θ_n in units of mb/sr^2 for $E_{in} = 200 \pm 10$ MeV. 79
6-13 Double differential cross section with respect to θ_p and θ_n in units of mb/sr^2 for $E_{in} = 300 \pm 10$ MeV. 80

List of Tables

4.1 Expected ranges of kinematic observables, based on E_{in} and range of θ_p. 51

5.1 θ_n ranges at beam height and solid angles for neutron bars. 59
5.2 θ_p ranges for E_{in} ranges used in analysis. 60
5.3 N_{inc} for the energy ranges used in analysis. 62

6.1 Detector time resolution 66
6.2 Time uncertainties 67
6.3 Energy uncertainties for given values of E_{in}. 67

Chapter 1

Introduction

Nuclear physics is concerned with the interactions between nucleons (protons and neutrons). The two-nucleon force between a pair of nucleons is well understood, and two-nucleon interactions can be modeled effectively using the two-nucleon force. However, there is evidence that an interaction involving three nucleons cannot be modeled accurately using only the sum of the pairwise two-nucleon forces. A three-nucleon force is therefore expected.

Scattering experiments using a deuteron (^{2}H nucleus, often abbreviated as d) and either a proton or neutron (abbreviated p and n respectively) are the simplest three-nucleon experiments. A deuterated polyethylene target and a 200 MeV proton beam were used to measure the cross section of the $d(p, pn)$ breakup reaction in [11]. A liquid deuterium target and a spallation neutron beam were used to measure the cross section of the neutron-deuteron elastic scattering reaction in [6]. The same target and neutron beam were used to measure the cross section of the $d(n, np)$ breakup reaction in [10].

This thesis describes an experiment conducted with essentially the same setup as [10]. We used a liquid deuterium target and a spallation neutron beam. Detectors measured the energies of the incident neutron, scattered neutron and scattered proton, and the scattering angles of the scattered neutron and proton. These variables constitute nearly the complete kinematics of the interaction, with the exception of the second neutron, which in quasielastic scattering (described below) leaves the interaction with relatively little kinetic energy.

1.1 Quasielastic Scattering

The specific interaction observed in this experiment is quasielastic scattering. The deuteron consists of a proton and a neutron, bound together by the two-nucleon force; quasielastic scattering occurs when the incident beam neutron interacts only with one of the two nucleons in the deuteron (in our case, the proton). The incident neutron and the proton are scattered out, carrying the kinetic energy of the incident neutron; the neutron that was inside the deuteron acquires little or no energy from the interaction. Because the result of the interaction is similar to what would happen if the proton were free, this is also called quasi-free scattering.

The difference between the quasielastic scattering we observe, and elastic neutron-proton scattering, is mainly in the initial conditions. The proton inside the deuteron has significant momentum even when the deuteron is at rest (measured in [2]). Therefore, while the energies and angles of the scattered neutron and proton are strongly correlated in neutron-proton elastic scattering (knowing the incident neutron energy and any one of the other values determines all the others), we expect the energies and angles of the scattered neutron and proton in our experiment to vary more.

Chapter 2

Experimental Setup

The basic components of our experiment were a neutron source, a beam monitor to measure the neutron flux, a liquid deuterium target, and detectors to measure the energies and directions of particles coming out of the target.

2.1 Neutron Beam Source

The experiment used a spallation neutron source at the Los Alamos Neutron Science Center (LANSCE). The LANSCE proton linear accelerator produces a beam of 800 MeV protons, which impacts a tungsten target (called "Target 4") at the Weapons Neutron Research (WNR) facility, ejecting 20–30 neutrons per proton. These neutrons have a wide continuous range of energies and directions [8]. Beam tubes collimate the neutrons into narrow beams, a map of which is given as Figure 2-1; our liquid deuterium target was located on the 15R flight path, 15 degrees right from the proton beamline and 16.93 m from Target 4 (this distance was defined as L_0). This far forward angle gives us the full range of neutron energies produced at Target 4, up to 800 MeV; beamlines at larger angles receive fluxes with lower proportions of high-energy neutrons.

The protons arrive at Target 4 in micropulses with FWHM approximately 125 ps, separated by 1.8 μs. These micropulses are in turn grouped in macropulses 750 μs long, with the macropulse rate being typically 40 Hz [9]. As each proton micropulse passes through Target 4, spallation neutrons are generated and leave Target 4 as a neutron micropulse. This neutron micropulse has a longer duration (no more than 500 ps) due to the length of the tungsten target. The time of proton micropulse arrival at Target 4 is communicated to experiments as an electronic signal. We use this electronic signal as t_0, the time that the neutron micropulse leaves Target 4.

2.2 Fission Chamber Neutron Beam Monitor

A fission chamber was used to measure the flux of neutrons coming down the 15R beam tube. The fission chamber we used, designed specifically for WNR use (see [14]), consisted of an ionization chamber, with a ^{238}U deposit on one of a pair of parallel foils held at a 300 V potential difference. Incident neutrons can cause the ^{238}U to fission, producing charged fission fragments. The fragments ionize the gas in the chamber, and the resulting free electrons and positive ions are picked up by the foils and amplified. The height of the resulting pulse is used to discriminate fission events from natural alpha decays and non-fission neutron interactions, such as (n,α) reactions. The difference between the pulse time and t_0 allows us to use time-of-flight from Target 4 to the fission chamber to determine the kinetic energy of the neutron detected.

2.3 Liquid Deuterium Target

The liquid deuterium target we used was contained in a "pancake-shaped" cylindrical flask with diameter 12.7 cm (5 inches), thickness 1.27 cm (0.5 inches) and Aramica (a PPTA aramid polymer, also used for the target flask in [7]) windows of thickness 50.8 μm (2 mils) each. To achieve thermal insulation, the target flask was placed inside a larger vacuum flask with a Kapton window of thickness 127 μm (5 mils). [6] The Mylar faces of the target flask bulged out significantly, doubling the actual thickness of the flask to approximately 2.5 cm at its thickest part. Furthermore, continuous boiling of the liquid deuterium created bubbles inside the flask, reducing the actual thickness of the target. The effective thickness of the target was therefore uncertain and was determined using deuteron elastic scattering, as described in section 5.6.

2.4 Detector Layout

To obtain near-complete kinematics of the breakup reaction, we measured the time of flight of the incident neutron, scattered proton, and scattered neutron, and the scattering angles of the proton and neutron. In addition, a ΔE-E detector identified recoil deuterons from elastic scattering, and several small detectors were used for position calibration of the neutron and proton detectors. A top-down view of the layout is given as Figure 2-3.

2.4.1 Neutron Detectors

The neutrons scattered from the target were detected by a wall of vertical plastic scintillator bars, positioned on beam-left (left-hand side as seen looking down the beamline). We used 9 bars (N1 through N9, with N1 being closest to the beam), each 2 m tall and 10 cm square. A neutron would be detected when it interacted with a proton (or other nucleus) in the bar, causing the nucleus to recoil and deposit energy in the scintillator. The resulting flash of light would be detected by two photomultiplier tubes (PMTs) on the ends of the bar; the pulse heights could be combined to give the amount of energy deposited in the scintillator, and the pulse times could be used to obtain the location and time of the event on the bar.

The neutron wall had a total width of 90 cm, height of 2 m, and thickness of 10 cm. The front face of the neutron wall was 248.1 cm from the center of the liquid deuterium target at its closest point, and the wall was positioned 67.24° from normal to the beamline. The center of the neutron wall was 26.9 cm above the beam height, and the edges of the wall were 55.55° and 76.17° from the beamline.

2.4.2 Proton Detectors

Protons scattered from the target passed through a series of detectors on beam-right to measure their energy and track. In the order that a proton passes through them, these were: front plastic scintillator (DE1), front wire chamber (WC1), permanent magnets (PM1 and PM2), rear wire chambers (WC2 and WC4), and rear plastic scintillators (P1 and P2).

Kinetic energy of the protons was measured using time of flight between front and rear plastic scintillators; tracks were obtained using wire chambers. A pair of permanent magnets was placed between front and rear wire chambers with the intention that the track deflection could be used to measure the proton momentum, but this was not done in this analysis because the rear wire chambers were not usable for much of the experiment's run time.

Wire Chambers

We used delay-line readout drift chambers (commonly referred to as wire chambers) for tracking. These contain alternating anode and cathode wires, running parallel to one another in a common plane. The spacing between adjacent anode wires (or adjacent cathode wires) is 0.8128 cm. Each chamber contains four planes, of which two have wires running vertically (called X1 and X2, since they measure horizontal position) and two have wires running horizontally (Y1 and Y2). WC1 had 18 anode wires in its X planes and 36 anode wires in its Y planes (for an active area of 14.6 cm by 29.3 cm); WC2 and WC4 had 74 anode wires in their X planes and 30 anode wires in their Y planes (for an active area of 60.1 cm by 24.4 cm).

A charged particle causes ionization in the chamber gas (65% argon and 35 % isobutane, run through isopropanol bubblers); the electrons released drift along the electric field towards the closest anode wire. When the electrons reach the anode, they cause an ionization avalanche where the large electric field accelerates the electrons to cause more ionization. The result is a cloud of electrons and positive ions on the same side of the anode wire as the original event, with the electrons moving inwards and the positive ions moving outwards. This creates a pulse in the anode wire and a smaller one in the cathode wire closest to the event. The chambers we used are further described in [1].

The anode wires are connected by a delay line with outputs at both ends. The time difference between the two outputs identifies the wire, while the difference between the time sum and the time that the proton passed through the chamber plane (determined using scintillators) gives the time that it took the electrons to drift to the anode (the drift time), and thus the distance of the event from the anode (the drift distance).

Alternating cathode wires are connected together as “odd” and “even” groups. A differential amplifier is used to compare the pulses received on the two groups, determining whether the event occurred closer to an odd or an even wire. The amplifiers we used are described in [5].

The processing of the wire chamber signals is discussed in 3.5.

Magnets

Two permanent magnets were used to bend the proton tracks. These were dipole magnets constructed by fitting SmCo bar magnets in rectangular frames, giving a maximum field strength of approximately 0.3 T in each. A more detailed description of the magnets and the particle tracking code that was to be used with them is found in [3]. The magnetic field would bend a proton away from the beamline, with lower-momentum protons being bent by larger angles. The field gap of the magnets (the region between the SmCo magnets where the field was roughly uniform) was 27.7 cm wide and 6.7 cm tall.

The effect of the magnets on our analysis is to cause our proton acceptance angle to shift with proton momentum, since our proton acceptance is limited after the magnets by the rear scintillators and wire chambers, but is defined before the magnets, in terms of the angles at which protons leave the target. Therefore our acceptance angle for low-momentum protons is somewhat closer to the beamline than our acceptance angle for high-momentum protons. This effect was measured in section 5.4.

2.4.3 ΔE-E Deuteron Detector

Recoil deuterons from elastic scattering were detected by a plastic scintillator (DE2) and a CsI scintillator. Both detectors were 9.6 cm square; DE2 was 2.5 mm thick, and the CsI detector was 14 cm thick. A charged particle would pass through DE2 and stop in the CsI detector, depositing energy in each detector. The relation between the two pulse heights depends on the particle mass and charge, allowing the elastic monitor to distinguish deuterons. The deuteron count rate can be used with the known elastic cross section to find the effective target thickness [13].

2.4.4 Position Calibration Detectors

Plastic scintillators were used for position calibration of the proton and neutron detectors. On the proton side, two small "finger" detectors were used for determining the physical locations of the wire planes (see section 3.6.2). On the neutron side, thin bars were used to calibrate the relation between top-bottom time difference and vertical position (see section 3.4.1).

A liquid scintillator detector was used with a plutonium-beryllium (PuBe) neutron source to calibrate the neutron bar ADCs.

2.5 Electronics and Data Acquisition

With the exception of the fission chamber, all detectors were read using a CAMAC system using 11 LeCroy 4300 FERA (Fast Encoding and Readout ADC) modules, with 16 channels each. All FERA modules were gated by a 290 ns pulse started by the master trigger, and wrote data to a LeCroy 4302 memory unit with a capacity of 16K data words. These data were in the form of an 11-bit integer (0 through 2047) and a status (underflow, valid, or overflow). The memory was read out at the end of every macropulse, since the macropulse spacing was large enough (25 ms, at the usual repetition rate of 40 Hz) to allow the entire contents of the memory unit to be read at once, a process taking 2-3 ms; readout would also be done if the memory unit was full.

Pulse height acquisition was done directly by passing the appropriate signal (possibly after amplifiers, gates or filters) to FERA. ADCs were generally adjusted so that zero inputs would appear as low values in the FERA range (a “pedestal”) without causing underflows, and high inputs would remain in range.

Timing acquisition was done by passing the signal (possibly after amplifiers, constant-fraction discrimination and/or delay lines) to NIM-to-ECL level translators, then to LeCroy 4303 TFC (time-to-FERA converter) modules whose outputs were fed to FERA modules; these TFCs were set for common start, with the master trigger as the start and the individual inputs as stop. This meant that a detector that did not fire during an event would appear as a FERA overflow.

The fission chamber was read by a separate CAMAC ADC; inputs to this ADC were the fission chamber output and a TAC that was started by the fission chamber and stopped by a delay of the t_0 pulse.

A set of CAMAC scalers was used as an independent system to count detector pulses without the overhead of the full data acquisition system. These scalers were read approximately once a second.

All three systems (FERA, fission chamber and scalers) were read by a computer running a Maximum Integration Data Acquisition System (MIDAS) [12] frontend, which simultaneously wrote the data to files in MIDAS format and passed it to an online analyzer.

Online analysis was done using a MIDAS/C++/ROOT analyzer program, while offline analysis was done by converting the MIDAS format first to text, then to ROOT trees.

2.5.1 Master Trigger

Possible trigger types were: neutron events, proton events, N-P coincidence, deuteron detector, cosmics, and PuBe. The first four of these required a t_0 pulse in coincidence; the other two were vetoed by t_0. Any one of these trigger types would cause a master trigger pulse, which both serves as the TDC common start and the beginning of the

ADC gate. The individual triggers were sent to dedicated TDCs so that we could determine which trigger(s) fired for a given event.

A neutron event was defined as pulses on both the top and bottom of any neutron bar, in coincidence with a t_0 pulse. This would correspond to a particle from the deuterium target (which could be a neutron, proton, deuteron or gamma) reaching the neutron wall. A rate divider was used so that a neutron event on its own would only trigger the FERA system on every 150th occurrence; otherwise these events would saturate the data acquisition system.

A proton event was defined as a coincidence of the front proton scintillator, DE1, with either of the rear proton scintillators, P1 or P2. Aside from accidental coincidences, this would correspond to a proton or deuteron from the target passing through the proton detectors. A rate divider was set to have only every 5th proton event trigger the FERA system.

An N-P coincidence would be the coincidence of a neutron event and a proton event. Since there could only be one charged particle emerging from the reaction at the target, this would guarantee that the particle arriving at the neutron wall was in fact a neutron, and so this trigger type would correspond to either deuteron elastic scattering or the desired breakup reaction. Because this trigger type represented the actual event of interest, it was not rate-divided. However, we discovered during data analysis that this trigger was not set up correctly.

The coincidence of the two detectors in the ΔE-E deuteron detector (DE2 and the CsI detector) was taken as the deuteron detector trigger.

The coincidence of at least 4 neutron bars (top and bottom) was considered a cosmic event, corresponding to a charged cosmic ray particle (most likely a muon) traveling through multiple neutron bars.

The coincidence of the liquid scintillator detector and at least one neutron bar was used as the PuBe trigger, meaning that a ^{9}Be(α,n) reaction and the subsequent decay of the excited state of ^{12}C had triggered both detectors simultaneously with a neutron and a gamma ray.

2.6 Experiment Run Periods

The experiment was run during the LANSCE beam periods in July, August and September 2009. The target flask was filled with liquid hydrogen during the July run, for the purpose of testing the experiment setup. Analysis of data taken with the liquid hydrogen target is done in the same way as analysis of data with the liquid deuterium target, but is not in the scope of this thesis.

The target was run either empty or filled with liquid deuterium for most of the August and September beam periods. The empty target data was collected to measure and subtract the event rate from scattering off of the target and vacuum flasks, and other backgrounds.

The MIDAS frontend saved data in blocks (typically of 2 hours length) called runs, which were assigned sequential run numbers: 1 through 581 for July and August data, and 600 through 786 for September data.

We selected sets of valid runs for the liquid deuterium target and for the empty target. Our criteria for valid runs were that detectors, electronics and data acquisition were functioning normally and stably throughout the run, the beam was on for at least part of the run, the permanent magnets were in position, and the target was either full (for liquid deuterium target runs) or empty (for empty target runs). These sets were concatenated to obtain two data sets.

The total duration of data taken with the liquid deuterium target is 345.75 hours; the total duration of data taken with the empty target is 114.92 hours. Both of these values represent time that the data acquisition was running; the actual beam time covered by the data is somewhat less, and the beam flux was also variable.

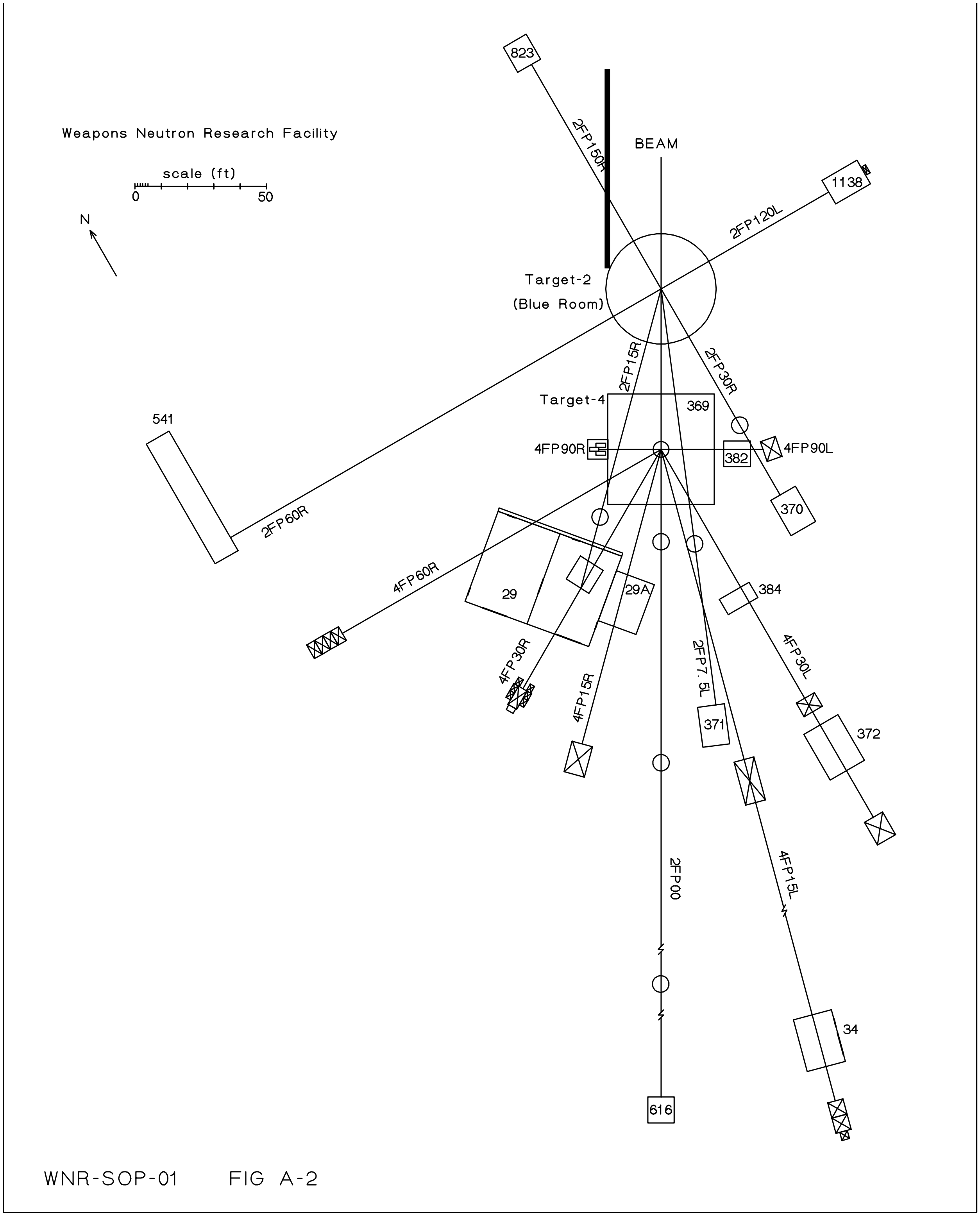
Weapons Neutron Research Facility
scale (ft)
0
50
N
823
2FP150R
BEAM
1138
2FP120L
Target-2
(Blue Room)
2FP15R
2FP30R
Target-4
369
541
4FP90R
382
4FP90L
370
2FP60R
4FP60R
29
29A
384
4FP30R
4FP15R
2FP7.5L
4FP30L
371
372
2FP00
4FP15L
34
616
WNR-SOP-01
FIG A-2

Figure 2-1: Flight paths at the Weapons Neutron Research facility, oriented with the proton beam pointing downwards.

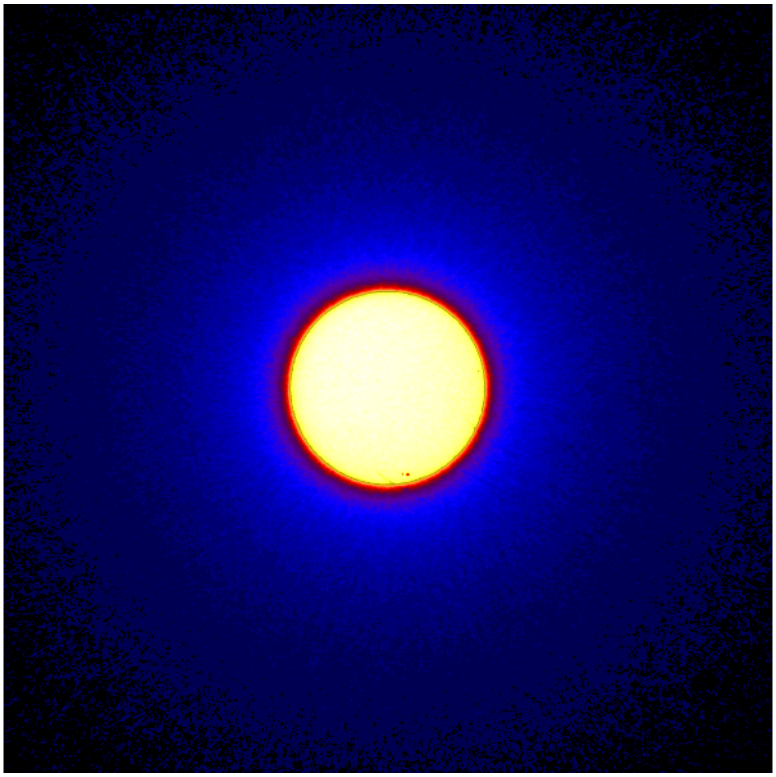

Figure 2-2: Neutron beam profile, measured with a phosphor image plate placed just upstream of the fission chamber. The actual width of this image is 10.16 cm (4 inches).

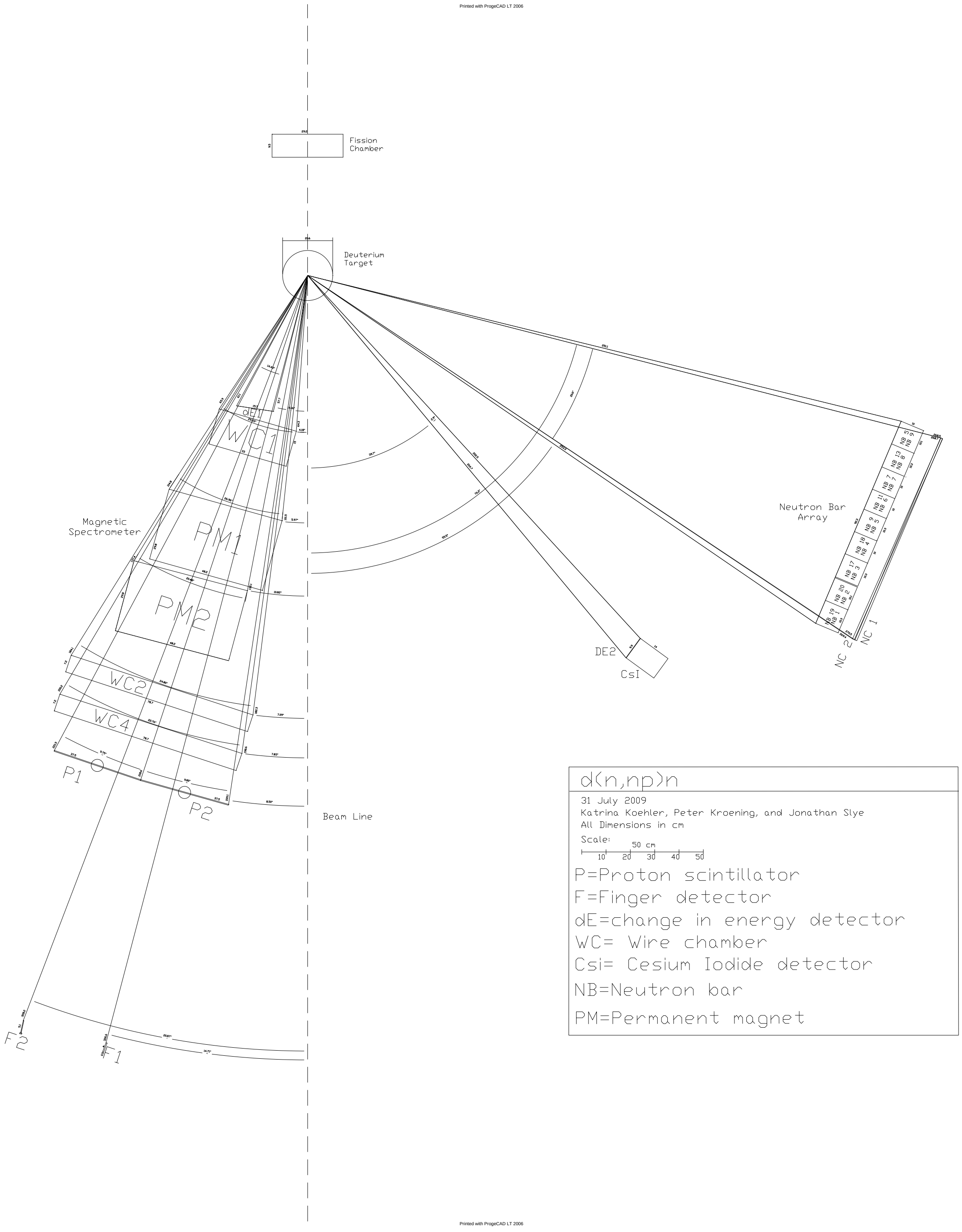
Printed with ProgeCAD LT 2006
Fission Chamber
Deuterium Target
Magnetic Spectrometer
dE1
WC1
PM1
PM2
WC2
WC4
P1
P2
F2
F1
Beam Line
DE2
CsI
Neutron Bar Array
NB 9
NB 5
NB 13
NB 8
NB 7
NB 7
NB 11
NB 6
NB 9
NB 5
NB 18
NB 4
NB 17
NB 3
NB 20
NB 2
NB 19
NB 1
NC 2
NC 1
d(n,np)n
31 July 2009
Katrina Koehler, Peter Kroening, and Jonathan Slye
All Dimensions in cm
Scale:
50 cm
10
20
30
40
50
P=Proton scintillator
F=Finger detector
dE=change in energy detector
WC= Wire chamber
Csi= Cesium Iodide detector
NB=Neutron bar
PM=Permanent magnet
Printed with ProgeCAD LT 2006

Figure 2-3: Detector layout, as seen from above.

Chapter 3

Detector Signal Processing

This chapter describes how the analysis program processes raw FERA data to obtain physically meaningful values — detector event times and event positions. We use the convention that calibration constants and constants of the experiment setup are in all capitals, and variables are in all lowercase. Most of the variables processed in the analysis are arrays of values (e.g. raw FERA values, which are stored in a 11 × 16 array, or neutron bar values, which are stored in arrays of 9), but we do not show the array indices here.

3.1 ADC Processing and Calibration

FERA modules add a pedestal current to the input signal so that a zero input gives a positive FERA channel. Furthermore, some inputs have constant offsets. These offsets must be subtracted before the FERA channel can be used as a measure of pulse size.

The FERA value corresponding to a zero input is directly observable, since ADCs have zero inputs for events where their corresponding detectors are not triggered. Provided that the pedestal current was positive and there was no overwhelming negative offset on the input, these zero-input events appear as a large, narrow peak in the FERA spectrum. The center of this peak is the ADC offset.

In order to convert the offset FERA channel number to a value of interest, such as energy deposited in a scintillator, a scale factor is needed. The scale factor is determined using events where the value of interest is known; for the neutron bars, for example, these events can be either ^{12}C transition gamma rays emitted from a PuBe neutron source, or minimum-ionizing cosmic rays. Both of these calibrations are described in [13].

3.2 TDCs and Time of Flight

Raw FERA channel values have to be converted to time relative to the FERA trigger. The TFC and FERA are linear over most of their range (tested using the process described in section 3.2.1), so this is done using a scale factor and an offset, similarly to the ADC calibration. We do not actually compute the scale factor and offset for TDCs.

The discrete FERA binning can cause problems in analysis; the integer FERA values are therefore converted to continuous values by adding random values in the range [-0.5,0.5[. This smooths the data without significantly increasing the error — the statistical error introduced by this is equal to the error of ±1 channel originally present in the discrete data.

After smoothing, the FERA channel values are used to obtain times relative to the master trigger. Each TFC module has two reference inputs. One channel is connected to a 40.6 ns delay of the master trigger pulse, and the other to a 165.5 ns delay. From the time calibrator results, we know that every channel in a single TFC module had equal scale factors and offsets (to within 1%), allowing us to interpolate between the FERA channel values for these inputs (tdc_{ref1} for the 40.6 ns reference, tdc_{ref2} for the 165.5 ns reference) to immediately convert from the raw FERA channel numbers tdc_{raw} to the calibrated times tdc_{cal} for all TDC inputs on every event.

$$tdc_{cal} = \frac{(165.5 - 40.6) * tdc_{raw} + 40.6 * tdc_{ref2} - 165.5 * tdc_{ref1}}{tdc_{ref2} - tdc_{ref1}} \tag{3.1}$$

The “raw calibrated” times tdc_{cal} are the times that signals entered the TFCs; this time is generally offset from the physically relevant time that a particle interacted with a scintillator or a scintillator flash reached the end of a neutron bar. These offsets are caused by inherent lags in the detectors and electronics, and delay lines that were added so that all time signals would arrive at TFCs within the FERA gate. The offsets, found in section 3.3, are subtracted from raw calibrated times to obtain calibrated event times.

Calibrated event times for single-PMT detectors represent the actual time of particle interaction with the detector, and can be subtracted from each other to obtain times of flight. Calibrated event times for neutron bar PMTs are offset so that the mean of the top and bottom event times gives the scintillator event time, and the top and bottom edges of the neutron bar give top-bottom time differences of equal magnitude. The errors in these times are known from the time offset calibration in section 3.3.

3.2.1 TDC Calibration

The scale factors were measured using a time calibrator. The time calibrator output pulses at a multiple of 10 ns after the master trigger pulse; connecting the time calibrator to the TFC inputs and running for a few minutes produced a series of sharp peaks on the FERA data, spaced by 10 ns (Figure 3-1). These peaks were checked for linearity, and the scale factor was obtained by choosing two peaks and dividing their FERA channel values by the known time separation. This was done for every channel of every TFC module.

3.3 Time Offsets

We determined offsets using the gamma flash. The spallation target emits a large amount of prompt gamma rays when a proton pulse hits it; these gamma rays travel down the beam tube and scatter off of the deuterium target. These gamma rays arrive at the detectors with a fixed delay relative to t_0, which is simply the total distance travelled divided by the speed of light. This “gamma flash” appears on every detector as a well-defined peak, separated in time from neutron or proton events. Thus it can

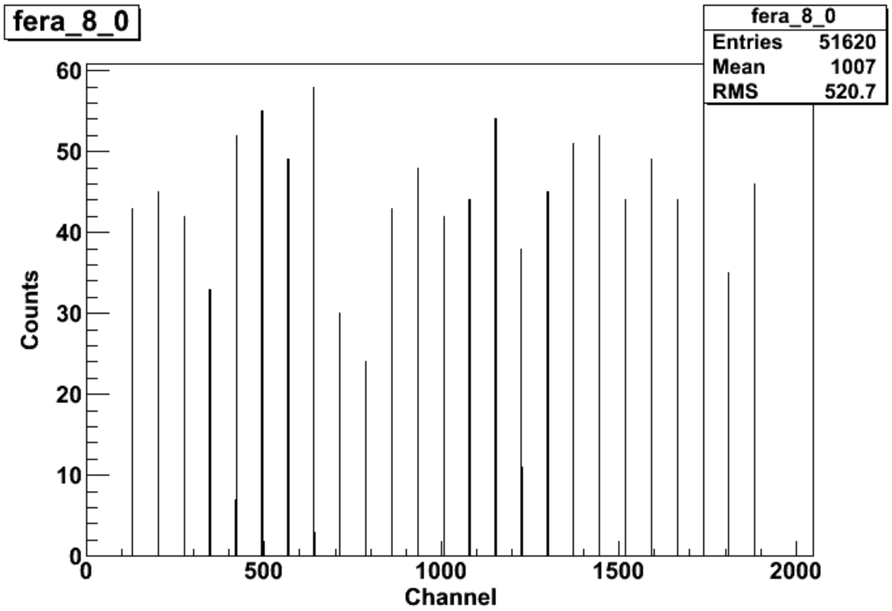

Figure 3-1: FERA channel numbers with time calibrator input, period 10 ns.

be used to determine the correct offset relative to t_0. Since the gamma flash is quite narrow, the width we observe for the gamma flash gives us a lower bound or worst case for the time resolution of the detector.

For every plastic scintillator, we computed the difference between the gamma time (the time we would expect a gamma flash to occur, based on the speed of light c) t_γ and the actual event time $t_{detector}$. t_γ depends on the distance $L_{detector}$ of the event from the liquid deuterium target; $L_{detector}$ is either a constant (for proton scintillators) or computed from the known event position (for neutron bars).

$$t_\gamma = t_0 + (L_0 + L_{detector})/c \tag{3.2}$$

Plotting $t_{detector} - t_\gamma$ gives a peak; the time offsets were set initially to center the peak approximately at zero.

Automatic Offset Correction

For various reasons (primarily small changes in the timing of the t_0 pulse), the required time offsets T_{OFF} shift over the course of the experiment. These shifts must be

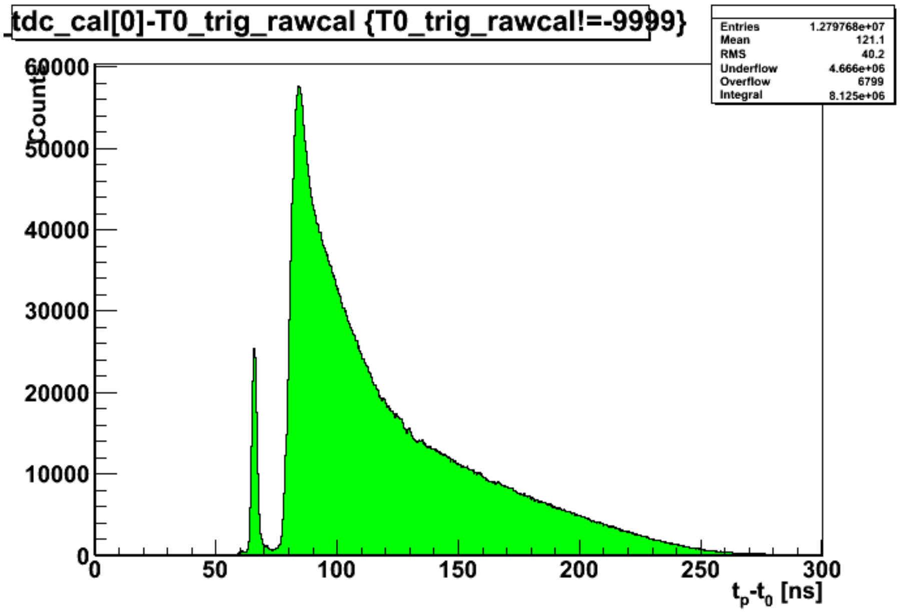

Figure 3-2: $t_{detector} - t_0$ for P1, with gamma flash at approximately 66 ns.

corrected precisely, since kinematics measurements are very sensitive to small (< 1 ns) shifts in time. The analysis program makes these corrections automatically.

If the magnitude of $t_{detector} - t_\gamma$ is within a cutoff value (set large enough to contain the whole gamma flash, but small enough to exclude massive particles), the event is considered a gamma event. If $t_{detector} - t_\gamma$ is positive, T_{OFF} is reduced by a small amount; if $t_{detector} - t_\gamma$ is negative, T_{OFF} is increased. Thus if there is a small shift in the required time offset, T_{OFF} will shift to keep the $t_{detector} - t_\gamma$ peak at zero.

$$T_{OFF} = T_{OFF} - (t_\gamma - t_{detector})SHIFT \tag{3.3}$$

The constant $SHIFT$ determines the amount of the shift; larger values of $SHIFT$ make this correction more responsive to changes in timing, but increase the jitter caused by the correction.

3.4 Neutron Bar Event Timing and Position

The times and positions of neutron bar events (the time when a neutron interacts with a scintillator bar) are found from the event times of the neutron bar top and bottom PMTs ($tdc_{N,top}$ and $tdc_{N,bot}$, respectively).

The neutron bar event time t_N is simply the mean of the two event times. This is because no matter where the event occurs, the light travel times to the two ends of the bar sum to the same value: the light travel time across the bar. The delay from the light travel time is included in the TDC offsets for the neutron bar PMTs.

$$t_N = \frac{1}{2}(tdc_{N,top} + tdc_{N,bot}) \tag{3.4}$$

The difference of the PMT event times is linearly related to the neutron bar event position. Two calibration constants A_N and B_N are used to obtain the event position as a height above the beamline, $y_{N,wall}$.

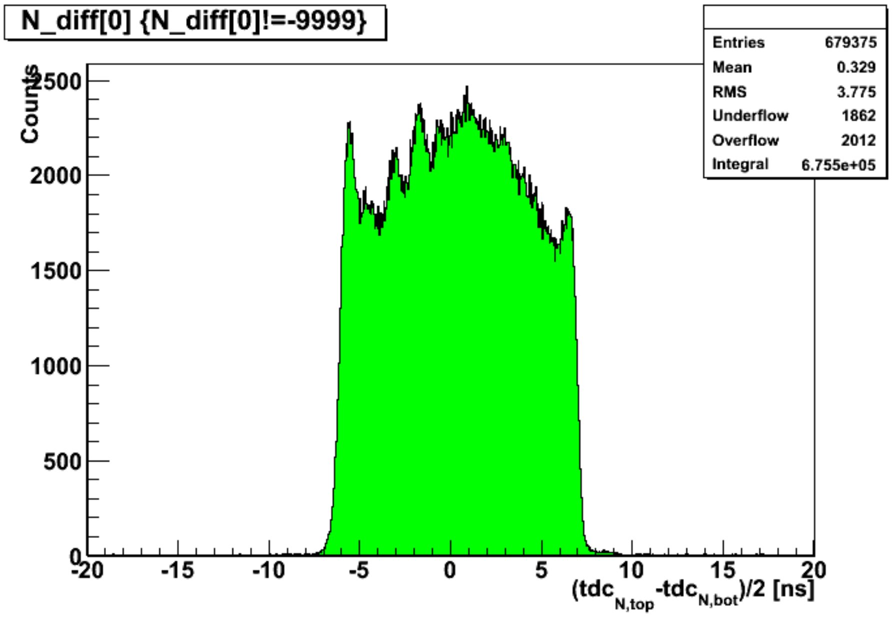

Figure 3-3: $\frac{1}{2}(tdc_{N,top} + tdc_{N,bot})$ for bar 1. The dips and peaks between -5 and 0 ns suggest that this time difference is not completely linear in position, introducing systematic error.

$$y_{N,wall} = A_N(\frac{1}{2}(tdc_{N,top} - tdc_{N,bot}) + B_N) \tag{3.5}$$

The height is simply the Y-coordinate of the neutron wall event position; the X and Z coordinates are randomly chosen to be anywhere in the scintillator bar. These coordinates are converted from detector rectangular coordinates to beamline rectangular and beamline spherical coordinates.

3.4.1 Neutron Height Calibration

The plastic scintillator bars behind the neutron wall are used as references of known height relative to the beamline. Histogramming the neutron bar PMT time differences for events that triggered a neutron calibration bar gives a peak of events where a particle from the target passed through both a neutron bar and the calibration bar; finding the peak centers for both calibration bars allows us to find the calibration constants for neutron bar event height.

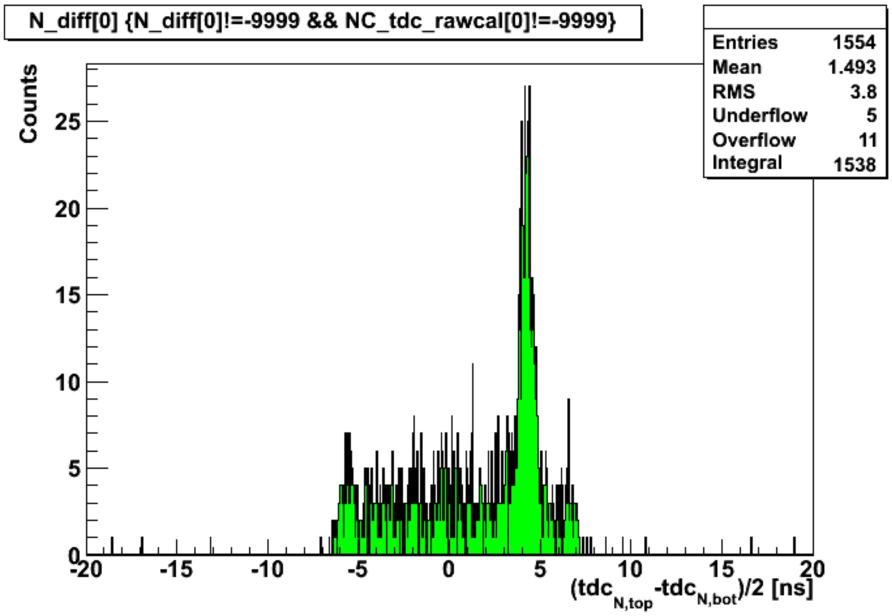

Figure 3-4: $\frac{1}{2}(tdc_{N,top} + tdc_{N,bot})$ for bar 1, integrating only events which trigger the first plastic scintillator bar.

Automatic offset correction (section 3.3) is used to keep the mean value of the

PMT time difference at zero.

3.5 Wire Chamber Signal Processing

The three components needed to determine the position of a wire chamber event are wire number, drift distance and drift direction. The first two are found from anode TDCs, and the drift direction is found from odd-even amplifiers (which read the wire chamber cathode signals). A wire plane can be either an X plane or a Y plane; here we consider an X plane, but a Y plane is processed identically (replacing “right” and “left” with “up” and “down”).

3.5.1 Determination of Wire Number

Plotting the difference between the TDCs at the two anode outputs of a wire plane gives a series of peaks, corresponding to the time for a pulse to travel down the delay line to the two ends. We calibrate this according to the method described in [1], fitting the peaks to a quadratic function. This gives us the wire number of the event. Figure 3-5 is an example of anode time differences, with the time differences corresponding to wires marked.

3.5.2 Determination of Drift Distance

The sum of the two anode TDCs, minus twice the time that the proton passed through the wire plane, is called the time sum; it equals twice the drift time of the ionized electrons from the event to the anode wire. The time that the proton passes through the plane is determined by taking the DE1 time and either the P1 or P2 time, and interpolating between the positions of those detectors to find the time at the wire plane.

The drift time is converted to drift distance using the drift time-to-distance function, which can be found from the accumulated data by using the fact that longer drift distances correspond to longer drift times and assuming that all drift distances

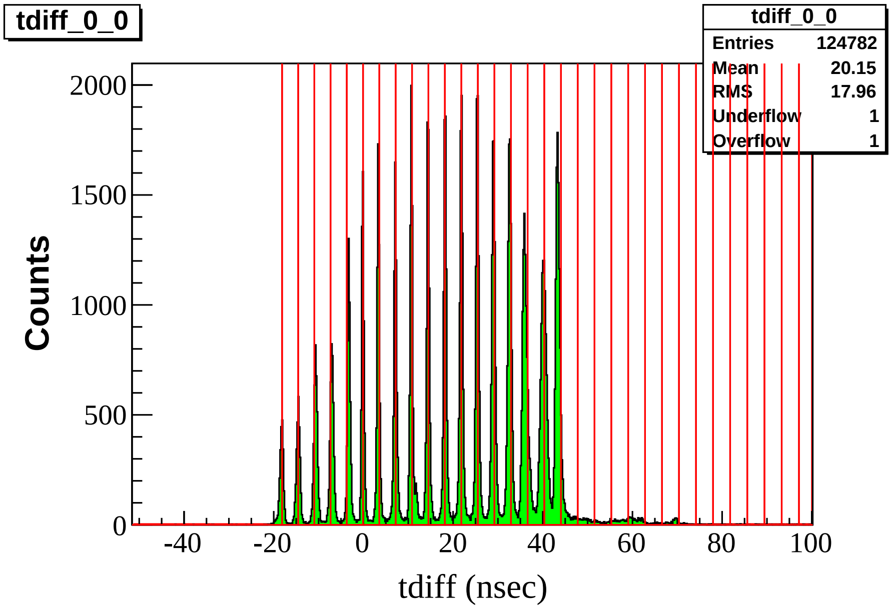

Figure 3-5: Anode time difference for WC1 X1 (run 420 data only). Red lines mark the time differences corresponding to wires, starting with wire 0.

are equally likely in the range between 0 and half the anode wire spacing. We histogram the drift times and integrate the histogram; if we normalize this integral so its maximum is half the wire spacing, it equals the time-to-distance function [4].

3.5.3 Odd-Even Amplifiers

The odd-even amplifiers have ADC outputs for the sum ("O+E") and difference ("O-E") of the odd and even signals. The O-E difference indicates whether the event was closer to an odd wire or an even wire; values under a cutoff (including FERA underflows) are "odd" events, and values over the cutoff (including FERA overflows) are "even" events. The odd-even cutoff is set at the median of the O-E distribution. The O-E amplifier gains shifted frequently, so this cutoff is corrected automatically as with the time offsets in section 3.3.

The O+E sum can be used as a threshold to cut out events where the difference is not large enough to distinguish between odd and even events, but this was not found to be necessary — events where the O-E signal is small are usually also events with

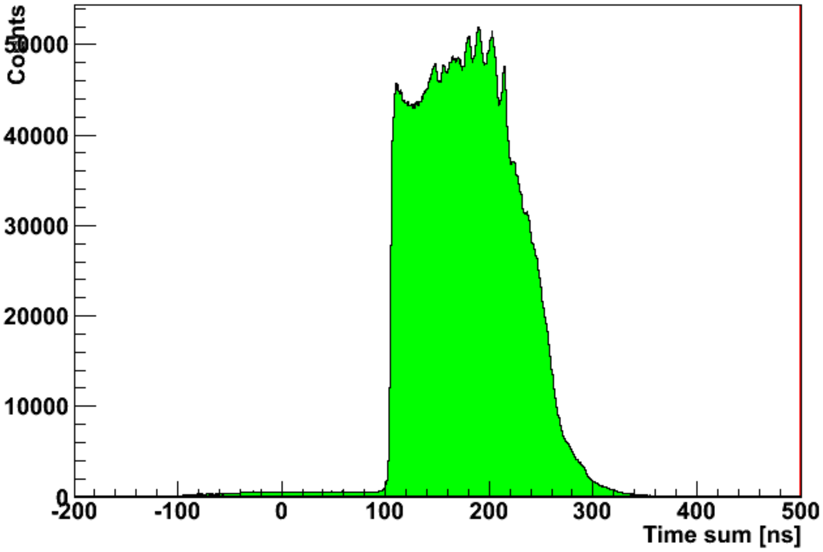

Figure 3-6: Time sum for WC1 X1, integrated over all liquid deuterium target runs.

small drift distances, where an incorrect O-E identification causes a small error in position. [5]

An "odd" event can have either a positive or a negative drift direction, depending on whether the odd cathode wire is left or right of the anode wire. This alternates — if a given anode has an odd cathode to its left, the adjacent anodes will have even cathodes to their lefts. Thus the drift direction is given by multiplying the odd-even identification oe by $(-1)^{wire\_number} OE\_MULT$, where OE_MULT is a constant of the wire plane that sets whether wire 0 has an odd or an even wire to its left. This gives us the drift direction of the event.

$$drift\_dir = oe * (-1)^{wire\_number} OE\_MULT \tag{3.6}$$

3.5.4 Wire Chamber Position

To obtain the wire plane coordinate (see section 3.6.1) of the event, we start with a "wire plane offset" $OFFSET_{WC}$ that corresponds to the wire plane coordinate of wire 0. The wire number adds a multiple of the wire spacing. The drift distance is

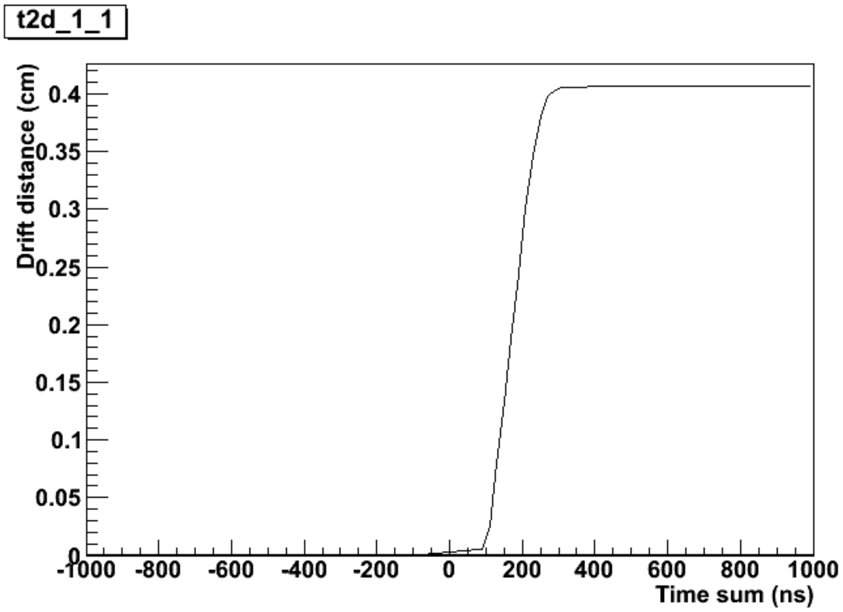

Figure 3-7: Time-to-distance function for WC1 X1.

multiplied by the drift direction, and added. This gives the wire plane coordinate.

$$x_{wc} = OFFSET_{WC} + WIRE\_SPACING * wire\_number + drift\_dist * drift\_dir \tag{3.7}$$

3.6 Tracking

3.6.1 Coordinate Systems

Particle tracking and kinematics is done in beamline coordinates. This is a coordinate system where the Z axis is the beamline (with downstream being the positive direction), the Y axis is vertical (up being the positive direction), and the X axis is horizontal (with beam-left being positive). Spherical coordinates (for kinematics) use the same Z axis; θ is the angle from the beamline, and ϕ is the azimuth (with $\phi = 0$ at the positive X axis). Individual position-sensitive detectors (wire planes and the neutron wall) use coordinates where the Z axis is normal to the detector face.

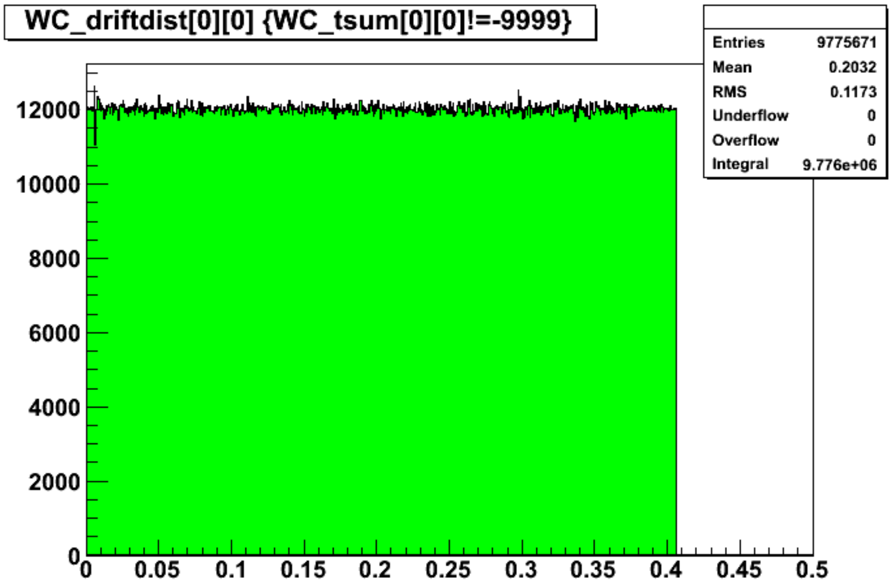

Figure 3-8: Drift distances (in cm) for WC1 X1, integrated over all liquid deuterium target runs.

3.6.2 Track Fitting

We expect that protons travel in straight paths before and after the magnets, so we fit a pair of straight tracks to front and rear wire chamber event positions.

Since all wire planes are roughly parallel to one another, the X and Y planes are used independently to find track slopes in each axis. The wire plane coordinates are rotated into beamline coordinates so straight tracks can be fit to them. The result is coefficients a and b such that the beamline rectangular coordinates of a proton track satisfy $x = az + b$ (for an X plane track) or $y = az + b$ (for a Y plane track).

If we had enough working wire planes to know the front and rear tracks, we would be able to use charged particle tracking through the permanent magnets (see [3]) to measure the proton momentum with more precision than is possible with time of flight.

The only track fitting result actually used in the analysis is the track found for WC1 X planes; the WC1 Y planes did not have working odd-even amplifiers, and the odd-even signals on WC2 and WC4 were unusable for part of the run period. We use

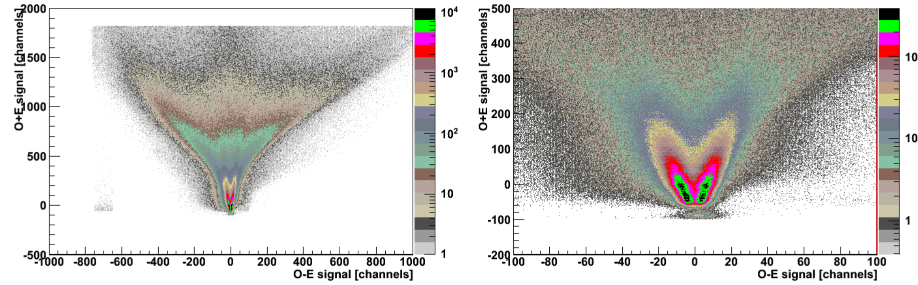

Figure 3-9: Odd-even amplifier outputs (in units of FERA channels) for WC1 X1 events where the WC1 X1 anode TDCs fired, integrated over all liquid deuterium target runs; the plot on the right is a zoomed version of the plot on the left. The O-E difference (X axis) is offset so that the cutoff between odd and even events is at 0.

a_x, the slope of this track, to determine θ_p — since the proton track is constrained to be within a few degrees of horizontal, $\theta_p \approx \tan^{-1} a$. b_x, the X-coordinate of the track at $z = 0$, is the horizontal position of the proton track as it crosses the plane of the liquid deuterium target.

Absolute Position Determination

To convert from wire plane coordinates to absolute position, we need the angle of each wire plane relative to the beamline, the distance of each wire plane from the deuterium target, and the offset of the zero coordinate of the wire plane from the beamline. The angle can be measured by directly measuring the alignment of the wire chambers, but the other parameters depend on the location of the wire planes inside the chambers, which is not known.

The location of the wire planes is found by two methods: finger detectors and wire-to-wire calibration. Both methods rely on tracking the straight paths of protons coming from the target to "project" a reference detector onto a wire plane; if we plot the wire plane positions of events where the reference detector fired, we see a peak that is the "shadow" of the reference detector. Because they rely on straight tracks, this calibration can only be done with the permanent magnets lowered.

Finger calibration uses as references the two small finger scintillators placed behind all of the proton detectors. These give us shadows on all of the wire planes; given the

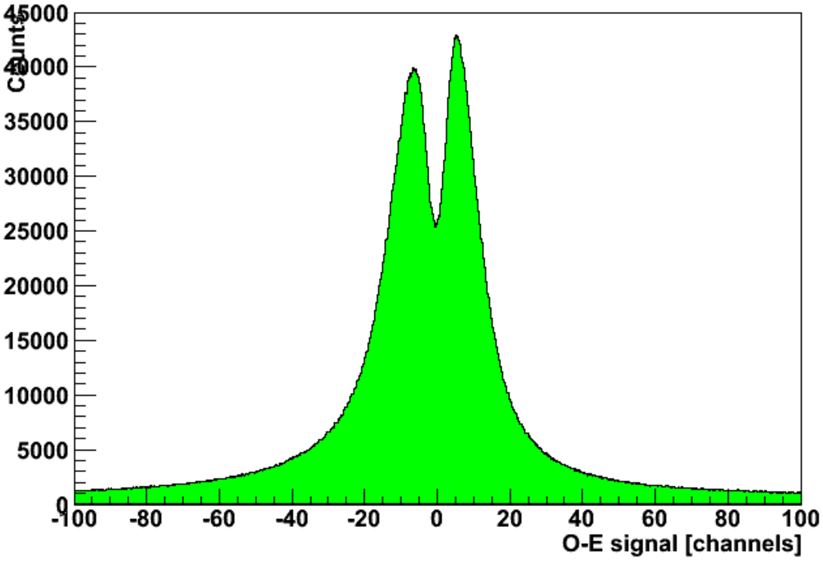

Figure 3-10: O-E difference for WC1 X1 events where the WC1 X1 anode TDCs fired, integrated over all liquid deuterium target runs.

position relative to the target of both fingers, and the angle relative to the beamline of the wire plane, this is enough to determine the distance and offset of the wire plane.

Because there are only two fingers — the minimum number needed — the results of this calibration are sensitive to errors in the measurement of finger position. These could be due to uncertainty in the physical measurement or statistical or systematic error in fitting the finger peaks.

Wire-to-wire calibration uses the wire planes to determine their location relative to one another. The rearmost wire plane in each axis is used as a reference; we plot the correlations between the wire number on this plane and the wire numbers on other planes. To find the relative position of a plane, we find, for each reference plane wire, the wire that has the most counts in coincidence with it. These are fit to a linear function that relates wire number in the reference plane to wire number in the plane being calibrated; we can now project any wire plane position to a position on the reference plane. Because of the larger number of points in this fit (30 or 74 wires, as opposed to 2 fingers), this is a much more precise result than the finger calibration, but it does not tell us the position of the reference planes.

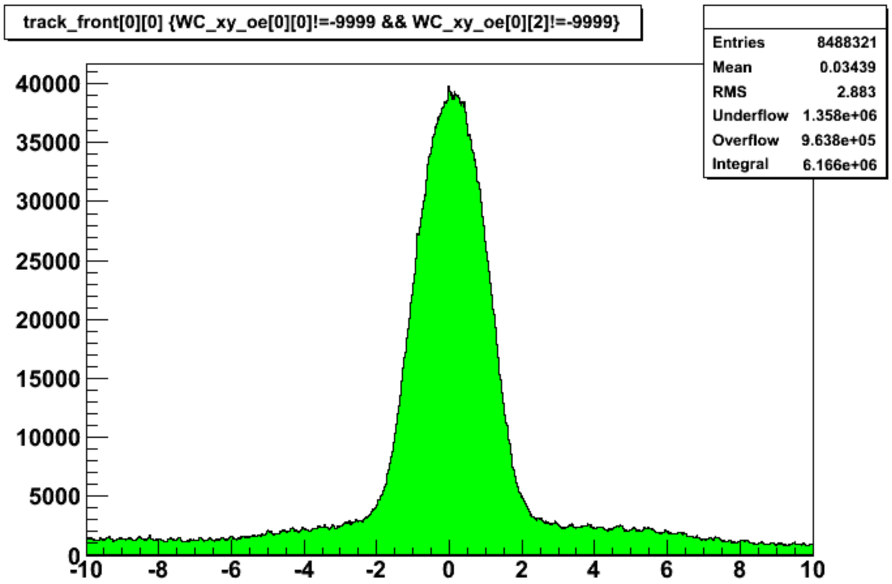

Figure 3-11: b_x for WC1 tracks, integrated over all liquid deuterium target runs.

The result from wire-to-wire calibration is combined with the finger calibration to get the final calibration. The linear functions obtained from wire-to-wire calibration are used to project the finger peaks in each wire plane back to the reference plane; then the reference plane position is determined using the same method used in finger calibration, but with a least-squares fit to the multiple finger peaks. Once the reference plane position is known, the other planes can be located.

Chapter 4

Determination of Event Kinematics

4.1 Determination of Scattered Proton Kinematics by Time of Flight

The proton kinematics are obtained from the calibrated event times of DE1 (t_{DE1}) and P1 or P2 (t_P). This data also allows us to compute the time of the scattering event in the deuterium target, and the energy of the incident beam neutron.

Given the event times and the detector distances L_P and L_{DE1} from the liquid deuterium target, the proton velocity $v_{p,tof}$, energy $E_{p,tof}$, and momentum $p_{p,tof}$ can be computed with the standard relativistic formulas as follows:

$$v_{p,tof} = \frac{t_P - t_{DE1}}{L_P - L_{DE1}} \tag{4.1}$$

$$\beta_{p,tof} = \frac{v_{p,tof}}{c} \tag{4.2}$$

$$\gamma_{p,tof} = \frac{1}{\sqrt{1 - \beta_{p,tof}^2}} \tag{4.3}$$

$$E_{p,tof} = (\gamma_{p,tof} - 1)m_p \tag{4.4}$$

$$p_{p,tof} = \sqrt{\gamma_{p,tof}^2 - 1}\, m_p \tag{4.5}$$

4.2 Correction for Proton Energy Loss in DE1

The velocity computed by Equation 4.1 is accurate for the proton as it travels between the two scintillators. However, the proton loses energy as it passes through detectors and other materials; if we want to compute the time the proton left the target, or the energy with which it left, we must correct for energy losses.

The main energy loss after the proton leaves the target is in the DE1 scintillator — other than the scintillators, the only materials in the proton flight path are thin membranes (wire chamber Mylar or target flask Kapton) or gases (air or wire chamber gas).

The DE1 ADC value adc_{DE1} gives us the amount of energy lost in the DE1 scintillator. Since the amount of light released in a scintillator depends on the energy deposited, and the PMT pulse is in turn proportional to the light release, the ADC value (after subtracting its zero value, given by the pedestal) is related to the energy loss. Therefore, the energy of the proton leaving the target E_p can be found:

$$E_p = E_{p,tof} + SCALE_{ADC,DE1}(adc_{DE1} - OFFSET_{ADC,DE1}) \tag{4.6}$$

The ADC offset $OFFSET_{ADC,DE1}$ is found as described in section 3.1. The ADC scale factor $SCALE_{ADC,DE1}$ is the value that causes E_p to best fit the quasielastic scattering kinematics described in section 4.4.

From this we obtain the other kinematics variables for the proton leaving the target:

$$\gamma_p = 1 + \frac{E_p}{m_p} \tag{4.7}$$

$$\beta_p = \sqrt{1 - \frac{1}{\gamma_p^2}} \tag{4.8}$$

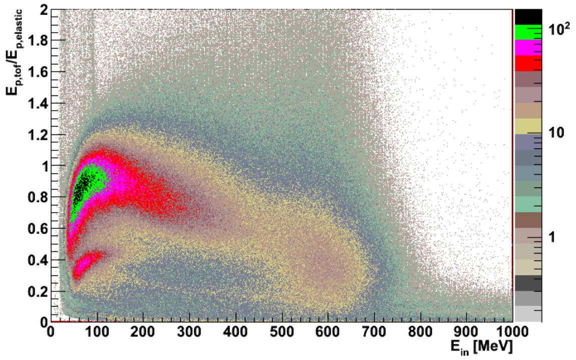

Figure 4-1: $E_{p,tof}/E_{p,elastic}$ dependence on E_{in}. Note the drop-off due to proton energy loss at low E_{in}.

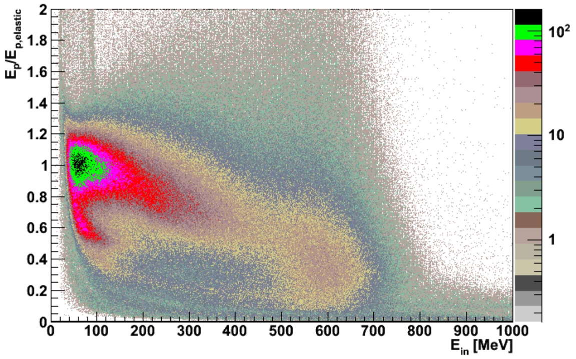

Figure 4-2: $E_p/E_{p,elastic}$ dependence on E_{in}, after the energy loss correction.

$$v_p = \beta_p c \tag{4.9}$$

4.3 Determination of Incident and Scattered Neutron Kinematics by Time of Flight

The scattering event time t_{in} is found by calculating the time of flight from the target to DE1:

$$t_{in} = t_{DE1} - \frac{L_{DE1}}{v_p} \tag{4.10}$$

The velocity of the incident neutron v_{in}, energy E_{in} and momentum p_{in} are computed in the same way as in section 4.1, but with flight distance L_0 and time of flight $t_{in} - t_0$.

The velocity of the scattered neutron can now be computed from the scattering event time and the neutron bar event time (t_N). The flight distance (r_N, the radial coordinate in the spherical coordinates found in 3.4) used here is variable, unlike the constant detector distances used in the proton and incident neutron kinematics. Thus the kinematic variables v_n, E_n and p_n are found again as in section 4.1.

4.4 Scattering Kinematics

Because we are observing quasielastic scattering, we expect the energies of the scattered proton and neutron to be close to those predicted from the incident neutron energy by elastic scattering kinematics. Of the three energies determined by time of flight, the incident neutron energy is the most precisely known because of the large flight distance; therefore we use E_{in} to predict values for E_n and E_p. These values are used in the scattering kinematics cut, discussed in section 5.1.3.

The formulas for computing $\gamma_{p,elastic}$ from E_{in} and θ_p, and $\gamma_{n,elastic}$ from E_{in} and θ_n are derived in [6]:

$$\gamma_{p,elastic} = \frac{(E_{in} + m_p + m_n)^2 + (p_{in} \cos\theta_p)^2}{(E_{in} + m_p + m_n)^2 - (p_{in} \cos\theta_p)^2} \tag{4.11}$$

$$\gamma_{n,elastic} = \frac{(E_{in} + m_p + m_n)^2 + (p_{in} \cos\theta_n)^2}{(E_{in} + m_p + m_n)^2 - (p_{in} \cos\theta_n)^2} \tag{4.12}$$

4.4.1 Expected Energies and Angles

We also use Equations 4.11 and 4.12 to predict the peak scattering angles and energies of the experiment. Our setup limits observable proton scattering angles to a much smaller range (approximately 8° horizontal and 2.5° vertical range) than neutron scattering angles (approximately 20° horizontal and 50° vertical range), so that the actually observed neutron scattering angles are restricted by the correlation to proton

Table 4.1: Expected ranges of kinematic observables, based on E_{in} and range of θ_p.

E_{in} [MeV]	100 MeV	200 MeV	300 MeV
E_n [MeV]	9.23-18.88	19.27-39.28	30.12-61.15
θ_n [°]	63.7-71.9	62.5-71.1	61.4-70.2
E_p [MeV]	81.25-90.91	160.99-181.01	239.26-270.29

scattering angles. θ_n can be computed from proton kinematics with the following equation, also from [6]:

$$\tan\theta_n = \frac{p_p \sin\theta_p}{p_{in} - p_p \cos\theta_p} \tag{4.13}$$

We can then compute the expected ranges of θ_n, E_p and E_n for the known range of θ_p. These appear in Table 4.1. These values neglect the momentum of the proton inside the deuteron, which will spread out the scattered energies and angles.

In elastic kinematics, $\phi_n = \phi_p + \pi$. Therefore, in quasielastic kinematics we expect the peak scattering angles to follow the same rule.

Chapter 5

Cross-Section Calculation

The basic formula for an energy-dependent cross-section $\sigma(E_{in}$ uses the number of observed events corresponding to the reaction of interest N_{obs}, the number of incident neutrons N_{inc} in the given energy range, the number of target nuclei per unit target area N_{target}, and the total efficiency of detectors and electronics ϵ.

$$\sigma(E_{in}) = \frac{N_{obs}}{N_{inc} N_{target} \epsilon} \tag{5.1}$$

5.1 Event Cuts

Various cuts were made to eliminate accidental coincidences and select only events to be counted in N_{obs}. The primary sources of background were gamma rays and neutrons. Gamma rays from the gamma flash constitute a well-defined background that can be easily removed. Neutrons and gamma rays from our beamline that scatter off of various materials in our setup arrive at detectors with unexpected timing and energies. Neutrons and gamma rays from other beamlines can also scatter into our experiment. These stray neutrons and gamma rays create an endless ocean of background events that are uncorrelated with the proton events.

5.1.1 Trigger Cuts

If the electronics had been working as intended, the N-P coincidence trigger would have corresponded to events of interest. However, we found that the N-P coincidence trigger seems to have occurred only when the proton event occurred after, or a short time before, the neutron event. Unfortunately, because of the scattering kinematics ($\theta_n > \theta_p$ means $E_p > E_n$), all the events of interest have the proton event occurring before the neutron event.

This could be explained by incorrect settings for pulse widths (proton singles trigger pulse width narrow, and neutron singles trigger pulse wide). Records of the setup do not include the relevant pulse widths, but do confirm that there was no significant delay used, which is consistent with what we see in the data. The correct setup would have had the proton trigger pulse wide.

The effect of this problem is that most N-P coincidence events are random coincidences of a real proton event with a background neutron event. It also means that the data as a whole is heavily skewed towards a small subset of events that did fall in the N-P coincidence, since all of coincidences were accepted while the proton singles rate divider caused only a fraction of the other physical events to be accepted. We therefore chose to analyze only events with the proton singles trigger type; this eliminates the bias.

5.1.2 Velocity Cuts

Gamma events (events whose time of flight relative to t_0 is exactly the light travel time) are rejected.

Events where a proton or neutron appears to have a negative velocity are rejected. These are most often accidental coincidences, where an upstream detector (such as DE1) and downstream detector (such as P1) interact with different particles.

5.1.3 Scattering Kinematics Cut

We expect the energies of the scattered proton and neutron to be related to the incident neutron energy by quasielastic scattering kinematics. Of the three energies determined by time of flight, the incident neutron energy is the most precisely known because of the large flight distance; therefore we test for physically reasonable events by comparing the observed scattered proton and neutron energies to those predicted from the incident neutron energy and the proton and neutron track angles.

We use the values computed in section 4.4 to make the following cuts: $E_n > 0.3E_{n,elastic}$, $E_{n,elastic} > 0.3E_n$. These are very loose cuts because we expect the actual scattered energies to deviate from the predicted values, due to the momentum distribution of the proton inside the deuteron. We do not expect this cut to eliminate all unphysical events.

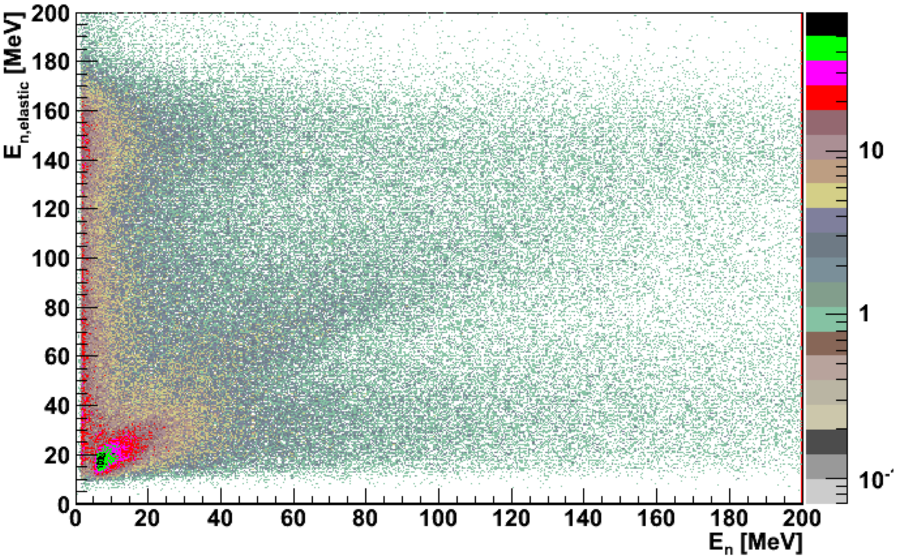

Figure 5-1: $E_{n,elastic}$ plotted against E_n. Note the diagonal band of quasielastic scattering events, and the vertical band of background events.

$E_{p,elastic}$ is not actually used for cuts because there is relatively little background on the proton side of the setup.

5.1.4 Proton Track Cut

Since proton tracking is significant in our analysis, we use a cut to ensure that only events with correct track identification are used. We use the constant value of the WC1 X planes track (see section 3.6.2), which corresponds to the horizontal distance of the track from the target center; only events where this distance is less than 5 cm are accepted.

5.1.5 Proton ADC Cut

An unexplained feature appeared in plots of the DE1 ADC against proton time of flight. Because we have no explanation for its existence and cannot compensate for it, and because it seems to be unphysical (it corresponds to the counts with low $E_p/E_{p,elastic}$ around $E_{in} = 550$ MeV in Figure 4-2), we rejected events in this "blob."

5.1.6 Rear Wire Chamber Cut

We measured the proton detector acceptance angle using WC4. This acceptance was limited on the beam-right side by the edge of WC4; therefore we accepted only events where WC4 X2 was triggered.

5.2 Background Subtraction

There is no way to distinguish between a good neutron wall event, caused by a neutron scattered from our target, from a background neutron wall event, caused by a neutron from another beamline. Instead we create a second data set by "mixing" proton data with neutron data from the next event.

The narrow band of breakup events with correlated neutron and proton kinematics is not visible in this data, but the background events are still visible because they never were correlated to begin with. Therefore we can subtract results from this mixed data from the results from the original data to remove the effect of the background.

The mixed data has a slightly different background event rate from the original data. This means that the mixed data has to be scaled to match the background rate of the original data; this background rate is determined by counting a set of unphysical events ($0.3E_n > E_{n,elastic}$) for both data sets.

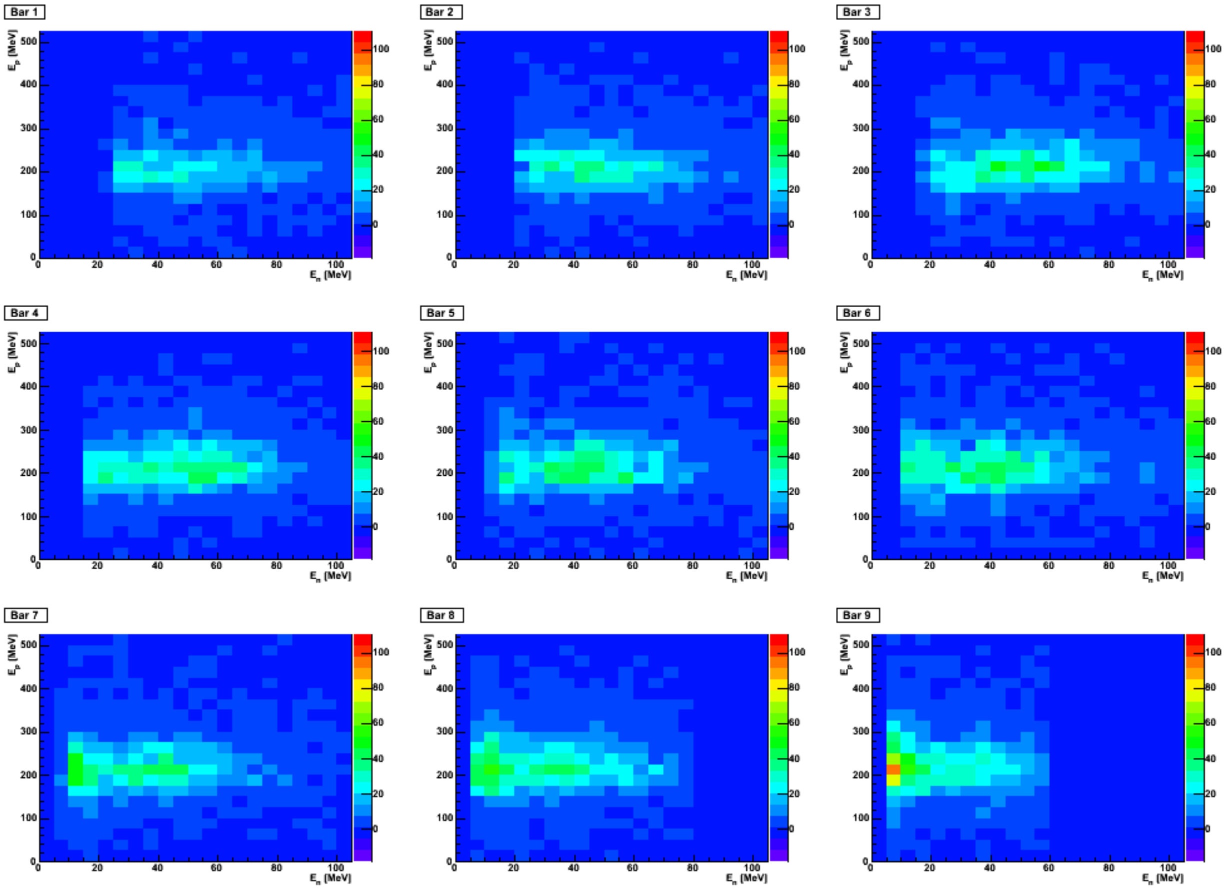

Figure 5-2: Event counts for neutron bars 1 through 9, plotted with respect to E_n (X axis) and E_p (Y axis), for $E_{in} = 300 \pm 10$ MeV and liquid deuterium target data.

5.3 Neutron Geometric Acceptance

The neutron wall geometric acceptance is simply set by the dimensions of the neutron wall. The θ_n ranges covered by each of the neutron bars are given in Figure 5.1, as are the solid angles Ω_n. These ranges are only correct at beam height; far above or below the beam height, the geometric acceptance of any given neutron bar shifts to

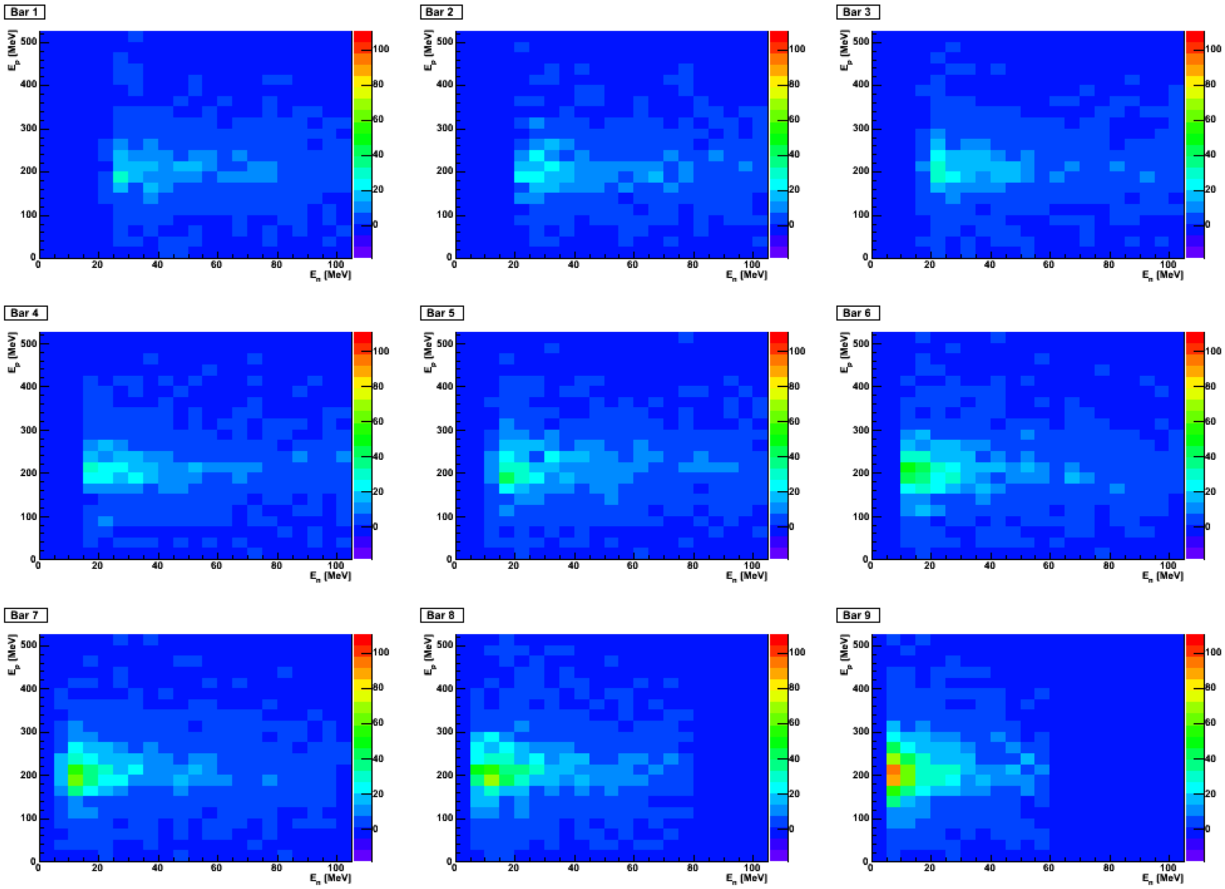

Figure 5-3: Quadruple differential cross section with respect to θ_p, θ_n, E_p, and E_n in units of mb/MeV^2/sr^2 for $E_{in} = 100 \pm 10$ MeV.

larger (by up to 4°) angles. However, most neutrons in breakup events have ϕ_n close to horizontal.

5.4 Proton Geometric Acceptance

The proton geometric acceptance is more complex; a proton track must pass through DE1, WC1, WC4, and P1 in order to be accepted by our cuts, and will be stopped if it intersects either the inactive region of a wire chamber or a permanent magnet. The magnets also bend the track so that the acceptance angle cannot be determined simply by looking at the physical layout of the setup, and even depends on the proton energy. The analysis by Ohlson [10] determined the proton acceptance by putting

Table 5.1: θ_n ranges at beam height and solid angles for neutron bars.

Bar number	θ_n [°]	Ω_n [sr]
1	55.55-57.20	0.0291
2	57.20-59.87	0.0289
3	59.87-62.07	0.0300
4	62.07-64.26	0.0299
5	64.26-66.79	0.0304
6	66.79-69.22	0.0302
7	69.22-71.32	0.0299
8	71.32-73.78	0.0303
9	73.78-76.17	0.0291

all measurements in a CAD program and finding the acceptance for straight proton tracks.

We chose to find the acceptance directly from the data by measuring the illuminated area of WC4. Looking at WC4, it is clear that the acceptance is limited on top by the permanent magnets, and on the bottom and beam-right by WC4. On the beam-left side, P1 events are limited by P1, but P2 events are limited by WC1. This means that the solid angle is roughly energy-independent for P1 events, since both of the horizontal boundaries are downstream of the magnets. This is not true for P2 events; the acceptance is smaller for lower energies, since protons that pass through WC1 get bent away from P2 and into P1.

For this reason we decided to use only P1 data. The loss in acceptance is small since the P2 acceptance is approximately 20% that of P1, depending on energy.

The vertical width of the proton acceptance is energy-independent, since the magnets do not bend proton tracks significantly in the vertical direction. We used WC4 Y2 to determine that the proton acceptance ranges from 0.50° to 2.70° below the beamline, independent of θ_p.

Because the $theta_p$ range in the proton acceptance shifts with E_p, it also shifts with E_{in}. We determined the range using WC1, by plotting the distributions of θ_p angles observed after applying all of the proton kinematics and acceptance cuts. The plots are given as Figure 5-4; the ends of the range were determined by taking the

Table 5.2: θ_p ranges for E_{in} ranges used in analysis.

E_{in} [MeV]	θ_p [°]
100 ± 10	17.1-25.0
200 ± 10	17.4-25.4
300 ± 10	17.6-25.6

midpoints of the left and right edges of the distributions and are given as Table 5.2.

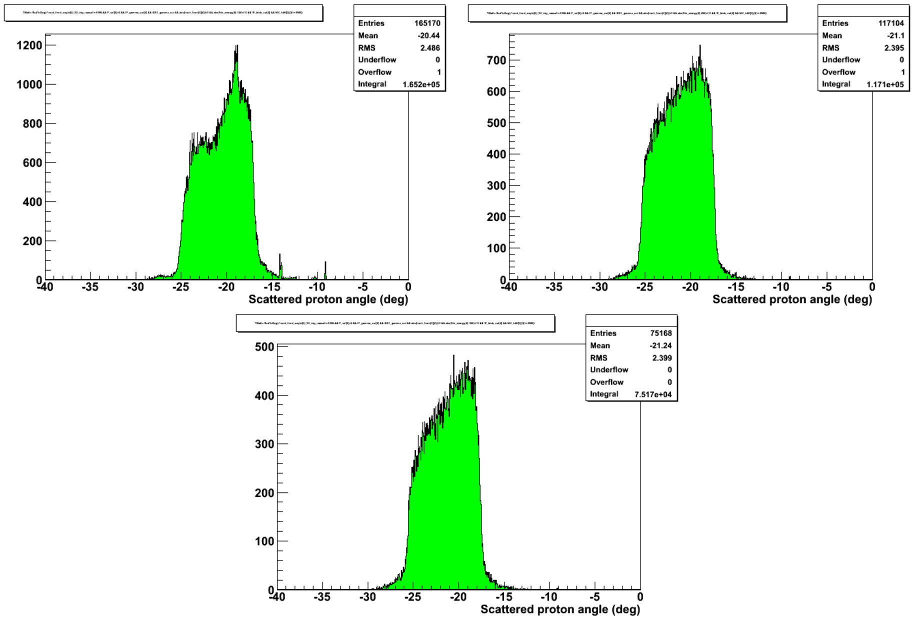

Figure 5-4: θ_p angles accepted at E_{in} ranges of 100 ± 10 MeV, 200 ± 10 MeV, and 300 ± 10 MeV.

From these measurements, we determine the solid angle of the proton geometric acceptance Ω_p to be 5.36×10^{-3} sr.

5.5 Detector Efficiencies

Plastic scintillators have near 100% efficiency for charged particles. The efficiency of the wire chambers we used was measured to be over 99% [3]. The proton track cut rejected 38% of otherwise valid events. The overall efficiency of the proton detectors as a whole is the product of these efficiencies, which is 62%.

The proton singles rate divider discarded a proportion of events; it was set to accept 1 in 5 events, but appears to have been malfunctioning to accept a lower fraction of events. We compare count rates on scalers whose inputs were taken before and after the rate divider; from this we determine the "efficiency" of the rate divider to be 17%.

The neutron bars have approximately 10% efficiency at normal incidence, according to [6]. This value depends on the neutron energy and an ADC threshold; setting an ADC threshold equivalent to 4 MeVee (1 MeVee being the amount of light produced when an electron loses 1 MeV of energy in the scintillator) removes the neutron energy dependence (a calibration of the neutron bar ADCs was done and is described in [13], but the threshold has not been applied in this analysis).

The neutron angle of incidence affects the neutron bar efficiency. Since the efficiency is largely limited by the probability of interaction between the neutron and the scintillator, a shallower angle of incidence increases the probability of interaction due to the larger path length. On the other hand, a shallower angle of incidence can reduce the amount of ionization which the recoil charged particle creates in the neutron bar, since the recoil particle may be more likely to pass through the bar to the neighboring bar before depositing all of its energy. These effects are difficult to account for without simulating the process in detail, so we chose to use 10% as the bar efficiency for all angles.

The dead time of the electronics and data acquisition adds another factor to the efficiency. The electronics were vetoed so that the master trigger would not fire while data was being read out of or written in to the FERA memory. This means that events that occurred during memory readout would not be saved in data. The resulting loss in efficiency should be observed as a ratio between the number of events stored in data and the number of trigger pulses seen by scalers. We have not been able to find a definite value for the dead time, so we use the dead time value of 85% observed in [6], an experiment with a similar event rate and electronics.

Table 5.3: N_{inc} for the energy ranges used in analysis.

E_{in} [MeV]	Liquid deuterium target N_{inc}	Empty target N_{inc}
100 ± 10	1.522e11	4.246e10
200 ± 10	1.094e11	3.047e10
300 ± 10	8.222e10	2.278e10

5.6 Flux and Target Normalization

The incident neutron flux N_{inc} was measured with the fission chamber. Fission events were identified by pulse height, and the incident neutron energies were measured by time of flight. The resulting spectrum, of detected events as a function of E_{in}, was scaled by the ^{238}U fission cross-section to obtain the spectrum of incident neutron flux as a function of E_{in}. This is described further in [13].

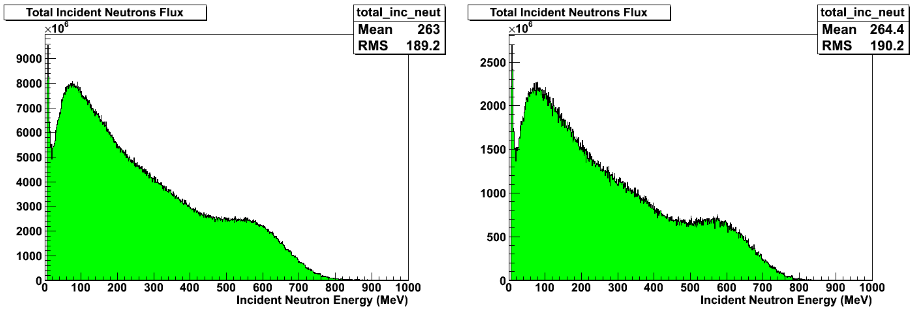

Figure 5-5: Incident neutron flux integrated over all runs with liquid deuterium target (left) and over all runs with empty target (right). The sharp peak at low energy may be either an artifact of the TDC or a 6.66 MeV resonance in the fission cross section (described in [7]).

The target thickness N_{target} was measured using the deuteron detector. Deuterons were identified using E-ΔE particle identification; the incident neutron energies for these deuteron events was determined using time of flight and elastic scattering kinematics. The rate of deuteron events as a function of E_{in}, the incident neutron flux measured by the fission chamber, and the known n-d elastic scattering cross section were used to determine the target thickness.

Unfortunately, this procedure finds the thickness of liquid deuterium in the target to be 5.1 ± 0.5 cm. This is incompatible with a direct physical measurement of the outside thickness of the target flask, which is 2.8 cm, so we use the direct physical measurement instead. This gives a target thickness of 0.14149 nuclei per barn.

Chapter 6

Results

6.1 Error Analysis

6.1.1 Time of Flight Energy Resolution

The time resolution of the scintillators is determined by measuring FWHM of the gamma flash for each; the standard deviation σ_t of the time measurement is then the FWHM divided by $2\sqrt{2\ln 2}$. For simplicity, we ignore the proton energy loss correction, and assume all time measurement errors are uncorrelated.

The gamma flash is probably not an accurate measure of the time resolution, because there is some amount of actual spread in the time that gamma rays hit a detector. The gamma flash is broader on neutron bars farther from the beamline, suggesting that a significant portion of the observed gamma flash width represents actual time spread (which would be expected to vary with θ) rather than properties of the detector and electronics.

The time of flight between the two proton scintillators is the difference of the two TDCs, and its error is independent of the actual times: $\sigma_{t_P - t_{DE1}} = \sqrt{\sigma^2_{t_{DE1}} + \sigma^2_{t_P}}$. t_{in} is also a linear function of the proton scintillator times ($t_{in} = \frac{t_{DE1}L_P - t_P L_{DE1}}{L_P - L_{DE1}}$), so its error is also constant; incident neutron and scattered neutron times of flight therefore also have constant error.

Given a time of flight t and a distance l, with time of flight error σ_t and distance

Table 6.1: Detector time resolution

Detector	FWHM (ns)
DE1	2.1
P1	2.6
N1	3.3
N2	3.5
N3	3.1
N4	4.8
N5	5.1
N6	5.4
N7	5.1
N8	4.9
N9	6.5

error σ_l, Ohlson [10] found the following formula for the energy error σ_E:

$$\sigma_E = mc^2(\gamma^3 - \gamma)\sqrt{\frac{c^2}{l^2}\sigma_t^2\left(1 - \frac{1}{\gamma^2}\right) + \frac{\sigma_l^2}{l^2}} \tag{6.1}$$

Using this formula, we obtain the values for σ_E plotted in Figure 6-1. σ_l is negligible for incident neutron and scattered proton energies, where σ_l/l is less than a percent, and much less than σ_t/t; we use $\sigma_l = 10/\sqrt{12} =$ cm (standard deviation for a uniform distribution of width 10 cm) for the scattered neutron. l for E_p is $L_{P1} - L_{DE1}$, l for E_{in} is L_0, and l for E_n is 148.4 cm, the minimum distance to the neutron wall. σ_t for the scattered neutron is computed using bar 9, which has the largest timing error and is therefore the worst case.

To obtain useful estimates of the uncertainties in our results, we use the values of E_n and E_p in Table 4.1 (using the largest value in each range) to obtain expected energy uncertainties; these are listed in Table 6.3. We find that E_{in} and E_n are determined with good precision (E_{in} because of its long flight path, E_n because E_n is relatively small), but E_p is very poorly determined.

Table 6.2: Time uncertainties

Detector	σ (ns)
P1-DE1	1.378
t_{in}	1.272
t_n	3.039

Table 6.3: Energy uncertainties for given values of E_{in}.

	100 MeV	200 MeV	300 MeV
E_n	3.68	9.91	17.42
E_p	22.02	66.16	128.67
E_{in}	2.25	6.84	13.49

6.1.2 Proton Angular Resolution

The position resolution of the wire planes is roughly 250 μm FWHM. This was determined by lowering the permanent magnets out of the proton flight path, fitting straight lines to the proton tracks, and measuring the deviations of individual wire plane positions from the tracks. The two WC1 planes were 9.43 cm apart, and proton incidence is close to normal, so the uncertainty in θ_p is 0.09°.

6.1.3 Neutron Angular Resolution

The horizontal position resolution of the neutron wall is simply determined by the neutron bar width of 10 cm. The vertical position uncertainty is estimated at 15 cm; the width of the distribution in Figure 3-4 suggests that the resolution is 6 cm, but irregularities in event height distributions (see Figure 3-3) suggest that there is additional systematic error. The horizontal uncertainty gives an uncertainty in θ_n of 1.3°, and the vertical uncertainty gives an uncertainty in ϕ_n of 3.4°.

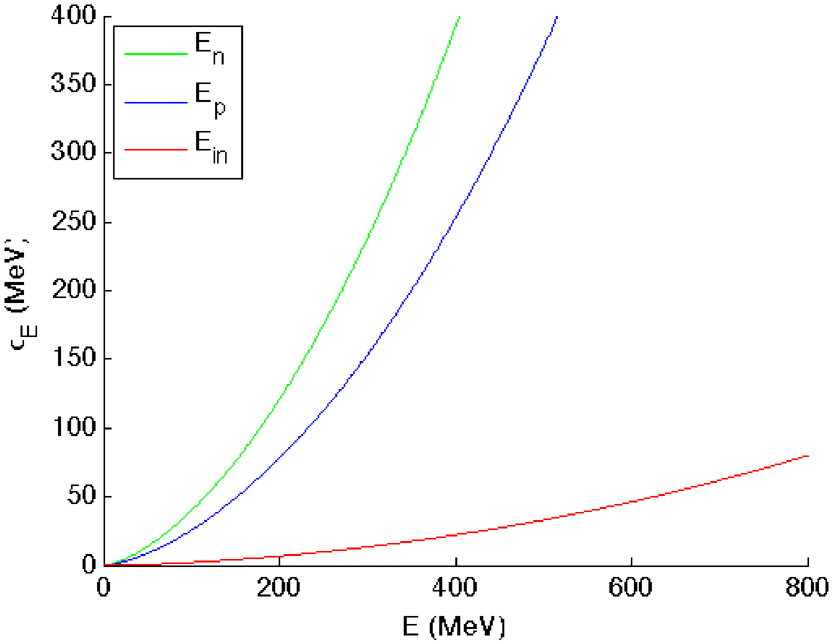

Figure 6-1: Uncertainty σ_E in time-of-flight energy measurement, as a function of energy E.

6.2 Energy-Dependent Cross Sections

To determine the differential cross section with respect to scattering energies and angles, we use 5.1, with additional scale factors corresponding to the energy bin widths and solid angles:

$$\frac{\mathrm{d}^4\sigma(E_{in})}{\mathrm{d}\Omega_p \mathrm{d}\Omega_n \mathrm{d}E_p \mathrm{d}E_n} = \frac{N_{obs}}{N_{inc}N_{target}\epsilon}\frac{1}{\Delta\Omega_p\Delta\Omega_n\Delta E_p\Delta E_n} \tag{6.2}$$

We use bin widths $\Delta E_p = 25$ MeV and $\Delta E_n = 5$ MeV, and plot E_p up to 525 MeV and E_n up to 105 MeV. $\Delta\Omega_p$ and $\Delta\Omega_n$ are the solid angles of the proton and neutron geometric acceptances. We compute cross sections separately for each of the neutron bars.

To better see the peak energies and statistical errors, we integrate over one of the energy variables. The bin widths are the same as for the quadruply differential cross sections.

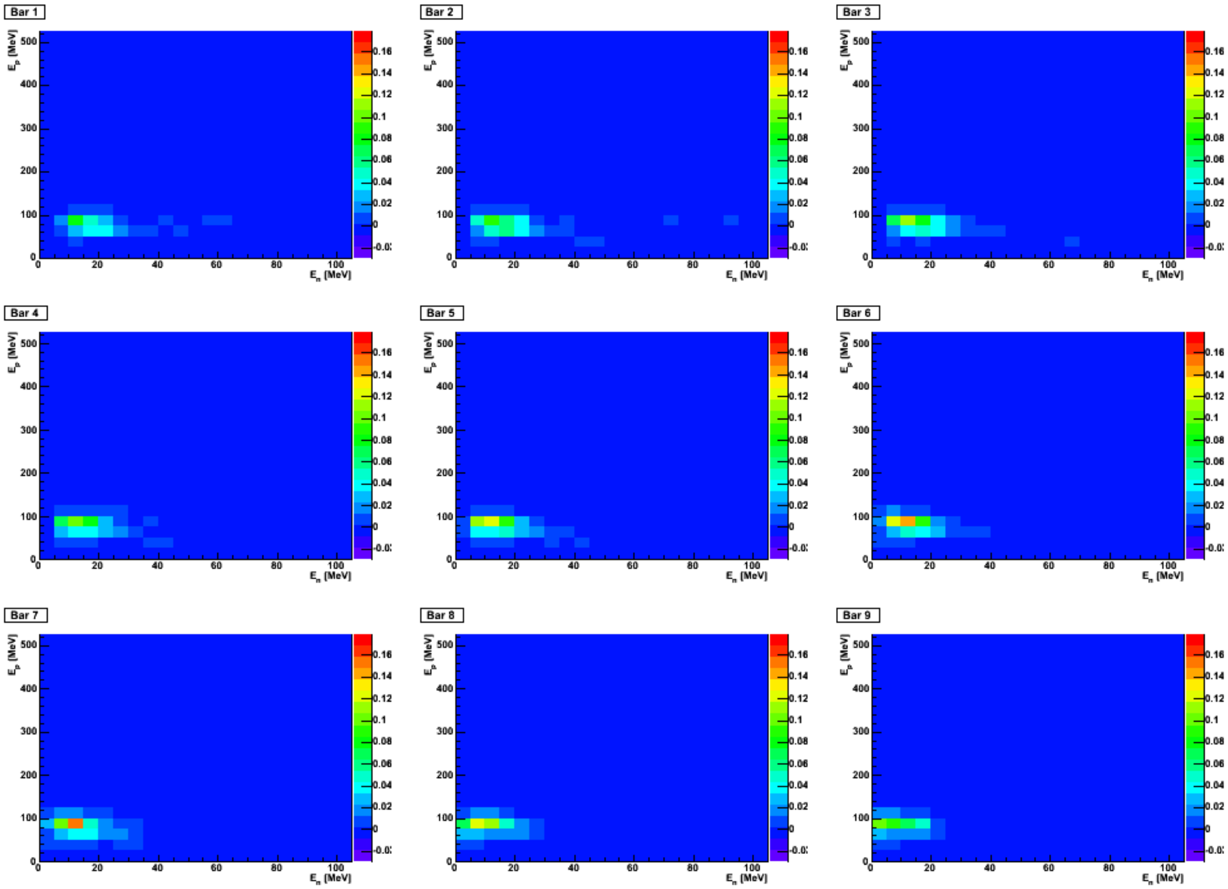

Figure 6-2: Quadruple differential cross section with respect to θ_p, θ_n, E_p, and E_n in units of mb/MeV^2/sr^2 for $E_{in} = 100 \pm 10$ MeV.

$$\frac{\mathrm{d}^3\sigma(E_{in})}{\mathrm{d}\Omega_p \mathrm{d}\Omega_n \mathrm{d}E_p} = \frac{N_{obs}}{N_{inc}N_{target}\epsilon} \frac{1}{\Delta\Omega_p \Delta\Omega_n \Delta E_p} \tag{6.3}$$

$$\frac{\mathrm{d}^3\sigma(E_{in})}{\mathrm{d}\Omega_p \mathrm{d}\Omega_n \mathrm{d}E_n} = \frac{N_{obs}}{N_{inc}N_{target}} \frac{1}{\Delta\Omega_p \Delta\Omega_n \Delta E_n} \tag{6.4}$$

6.3 Angle-Dependent Cross Sections

The cross sections measured in the previous section integrate over the entire solid angle of each neutron bar. We can do better, since we have ϕ_n. Therefore we can plot the dependence of the differential cross section on θ_n and ϕ_n. If we bin the cross

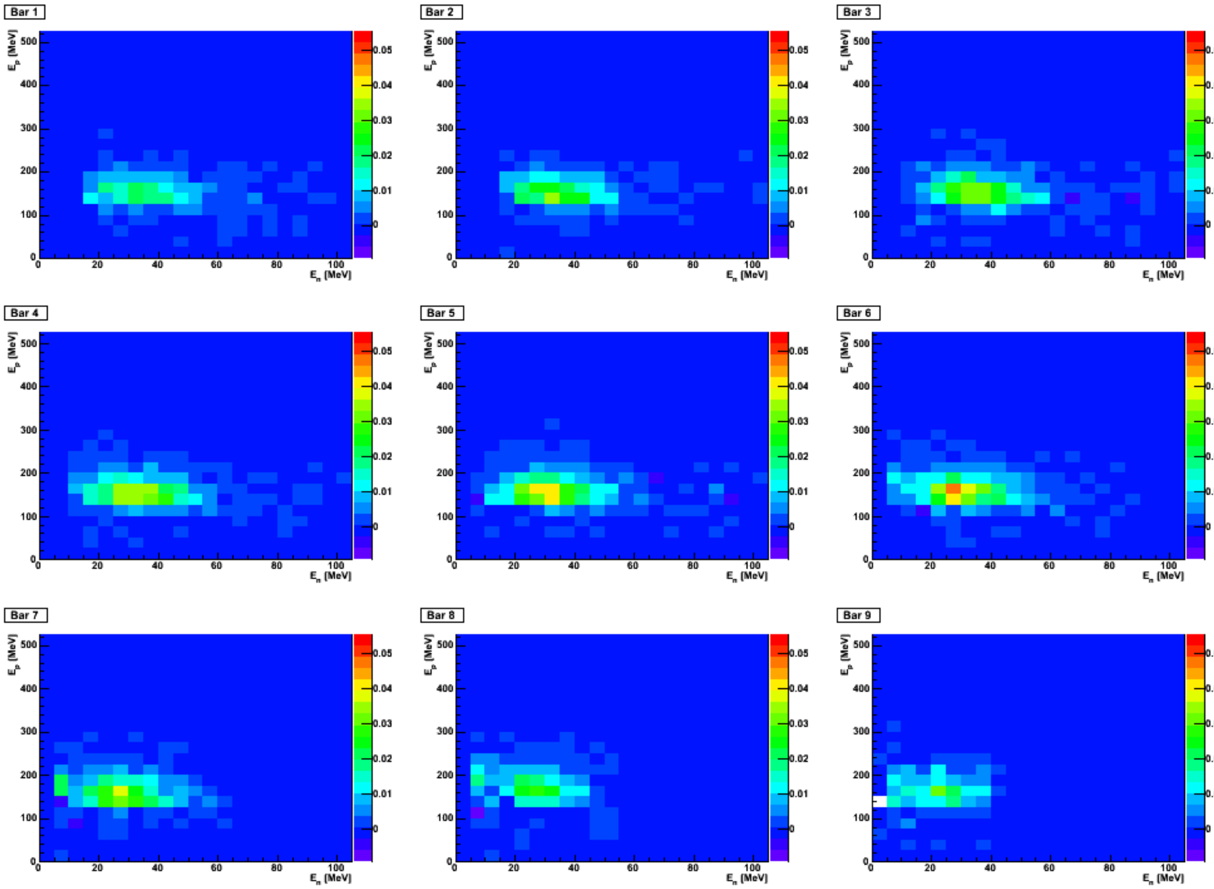

Figure 6-3: Quadruple differential cross section with respect to θ_p, θ_n, E_p, and E_n in units of mb/MeV^2/sr^2 for $E_{in} = 200 \pm 10$ MeV.

section in θ_n and ϕ_n, the solid angle corresponding to each bin has an additional factor of $\sin\theta_n$. For ease of presentation, we integrate over both E_p and E_n, making this a double differential cross section:

$$\frac{\mathrm{d}^2\sigma(E_{in})}{\mathrm{d}\Omega_p \mathrm{d}\Omega_n} = \frac{N_{obs}}{N_{inc}N_{target}\epsilon}\frac{1}{\Delta\Omega_p\Delta\theta_n\Delta\phi_n\sin\theta_n} \tag{6.5}$$

We see that the cross section is largest near the angles given in section 4.4.1, and that the width of the distribution decreases with increasing E_{in}. This is expected; as the scattered energy E_n increases, the random spread in momentum imparted by the internal momentum of the proton has a smaller effect on the direction of the scattered neutron.

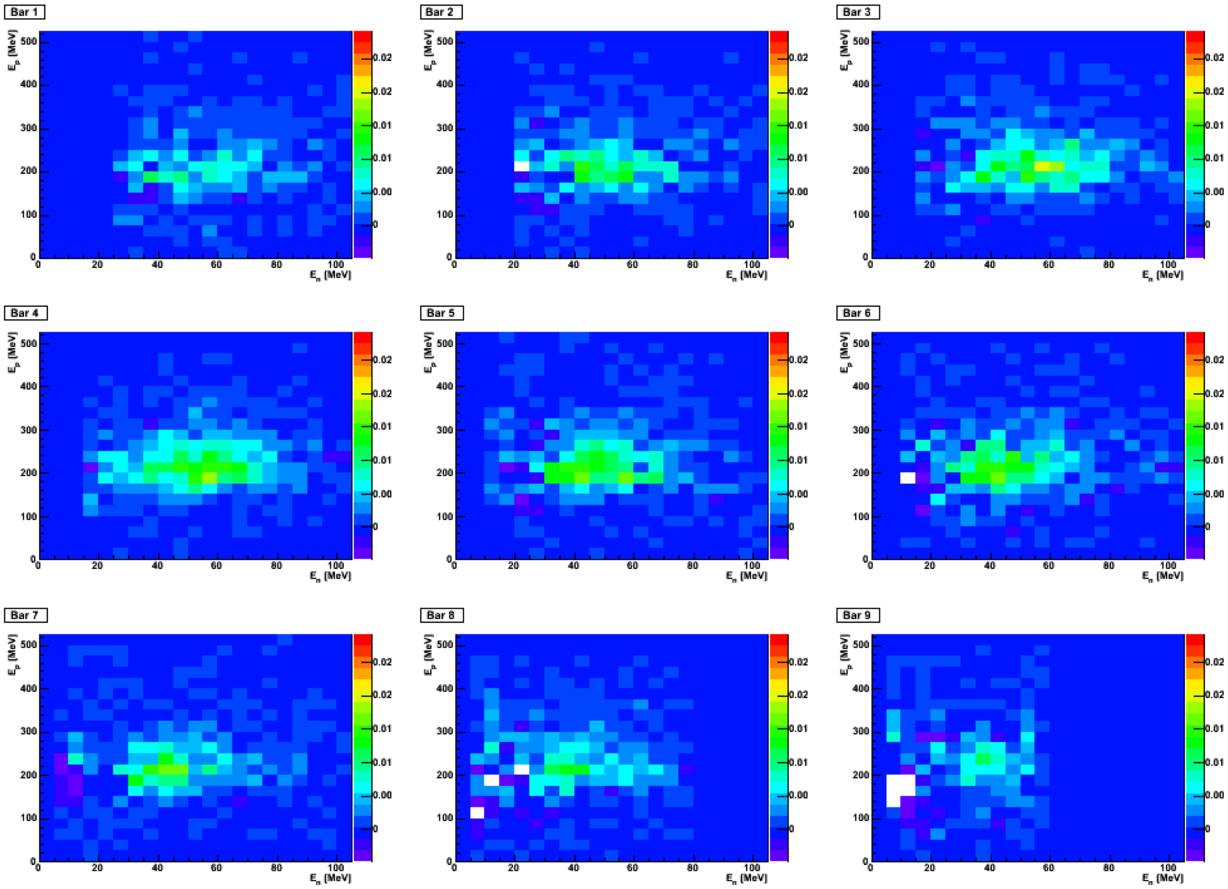

Figure 6-4: Quadruple differential cross section with respect to θ_p, θ_n, E_p, and E_n in units of mb/MeV^2/sr^2 for $E_{in} = 300 \pm 10$ MeV.

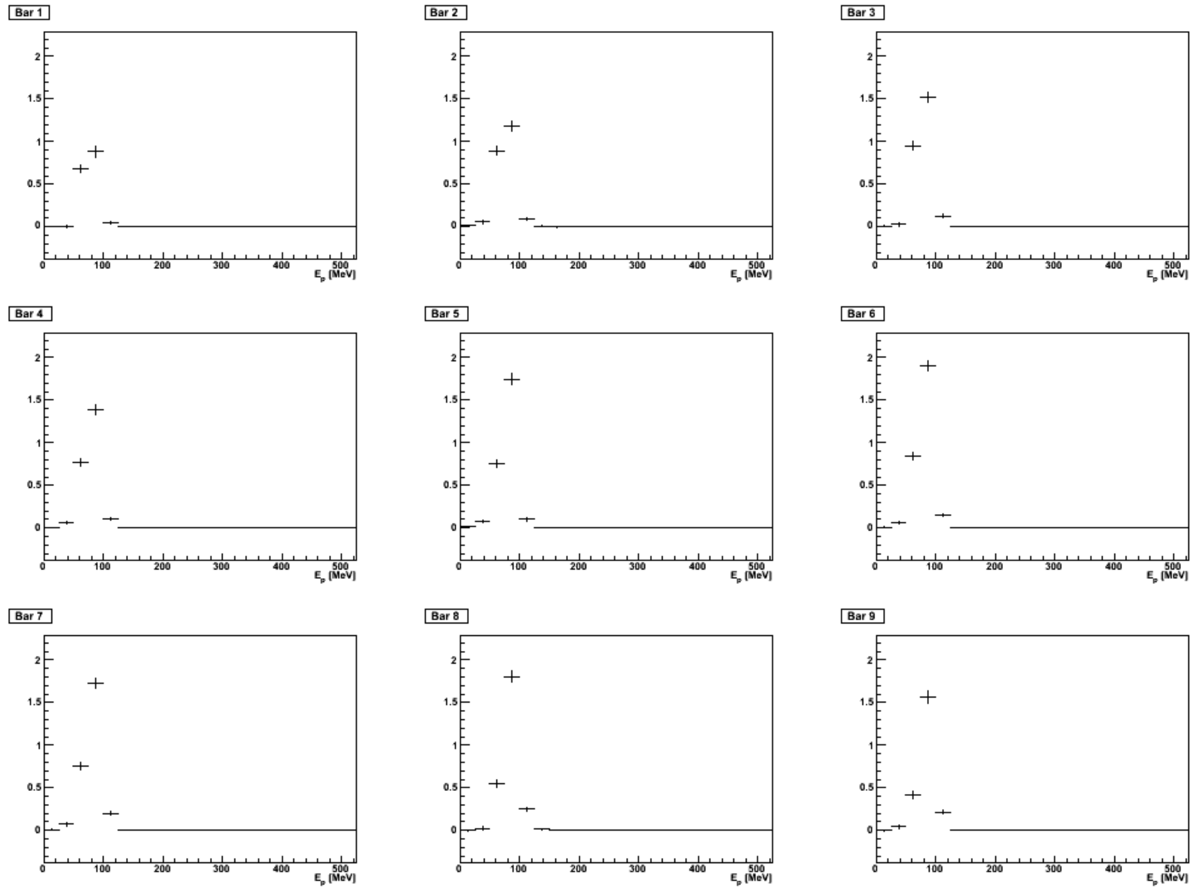

Figure 6-5: Triple differential cross section with respect to θ_p, θ_n, and E_p in units of mb/MeV/sr^2 for $E_{in} = 100 \pm 10$ MeV.

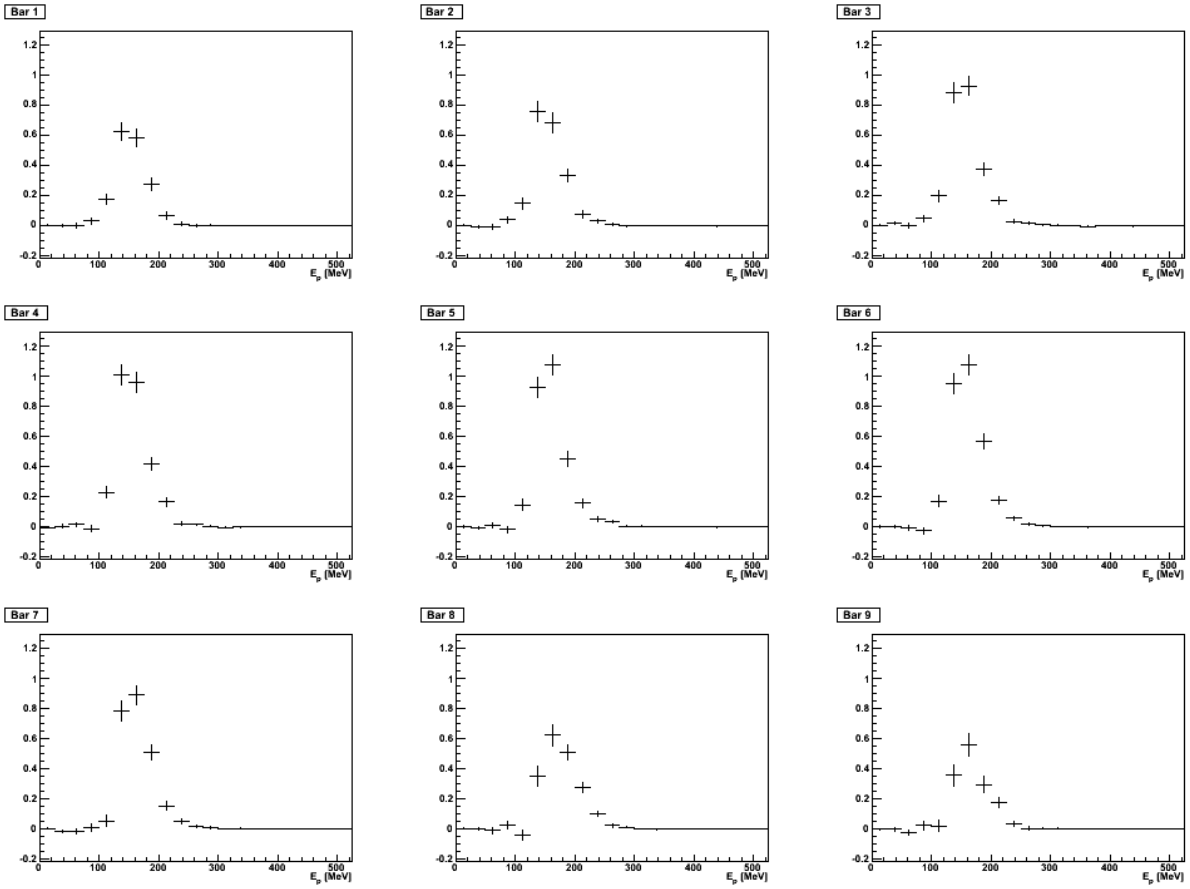

Figure 6-6: Triple differential cross section with respect to θ_p, θ_n, and E_p in units of mb/MeV/sr^2 for $E_{in} = 100 \pm 10$ MeV.

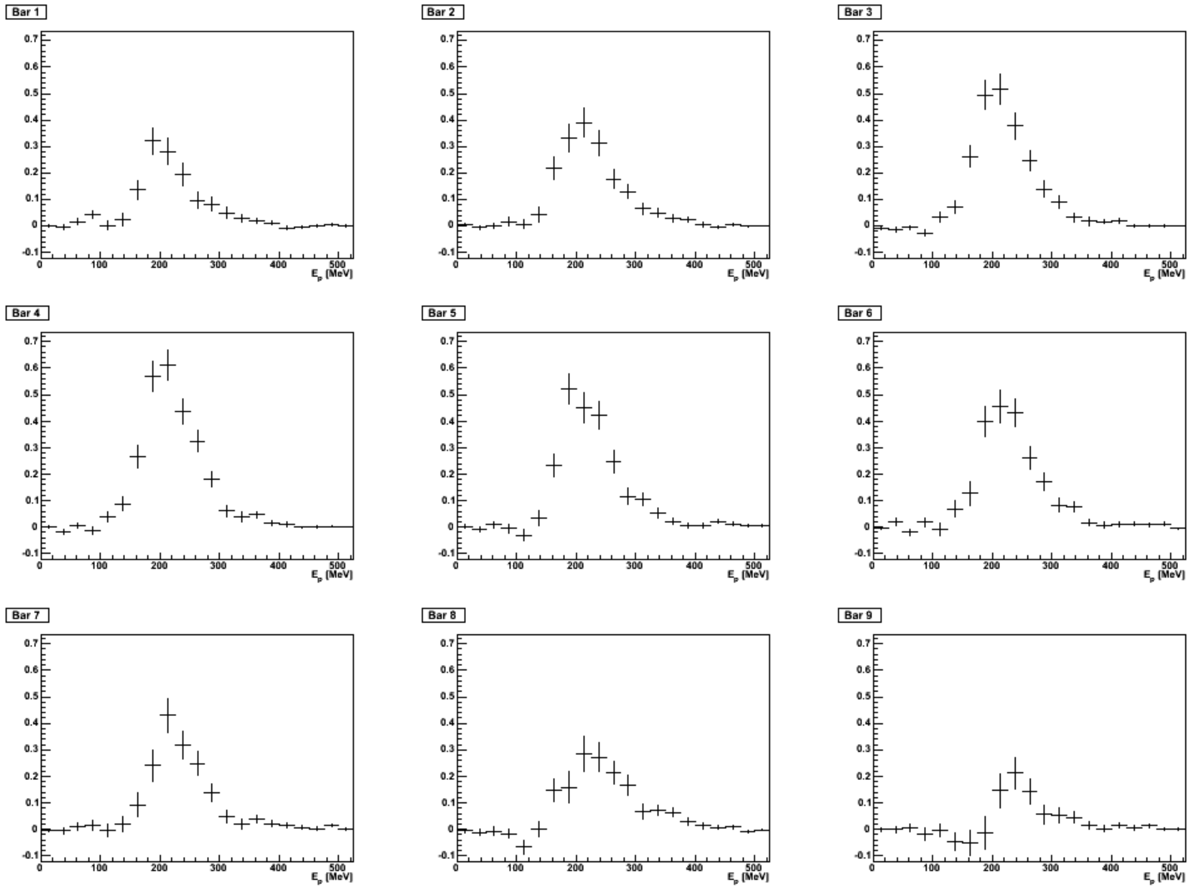

Figure 6-7: Triple differential cross section with respect to θ_p, θ_n, and E_p in units of mb/MeV/sr^2 for $E_{in} = 100 \pm 10$ MeV.

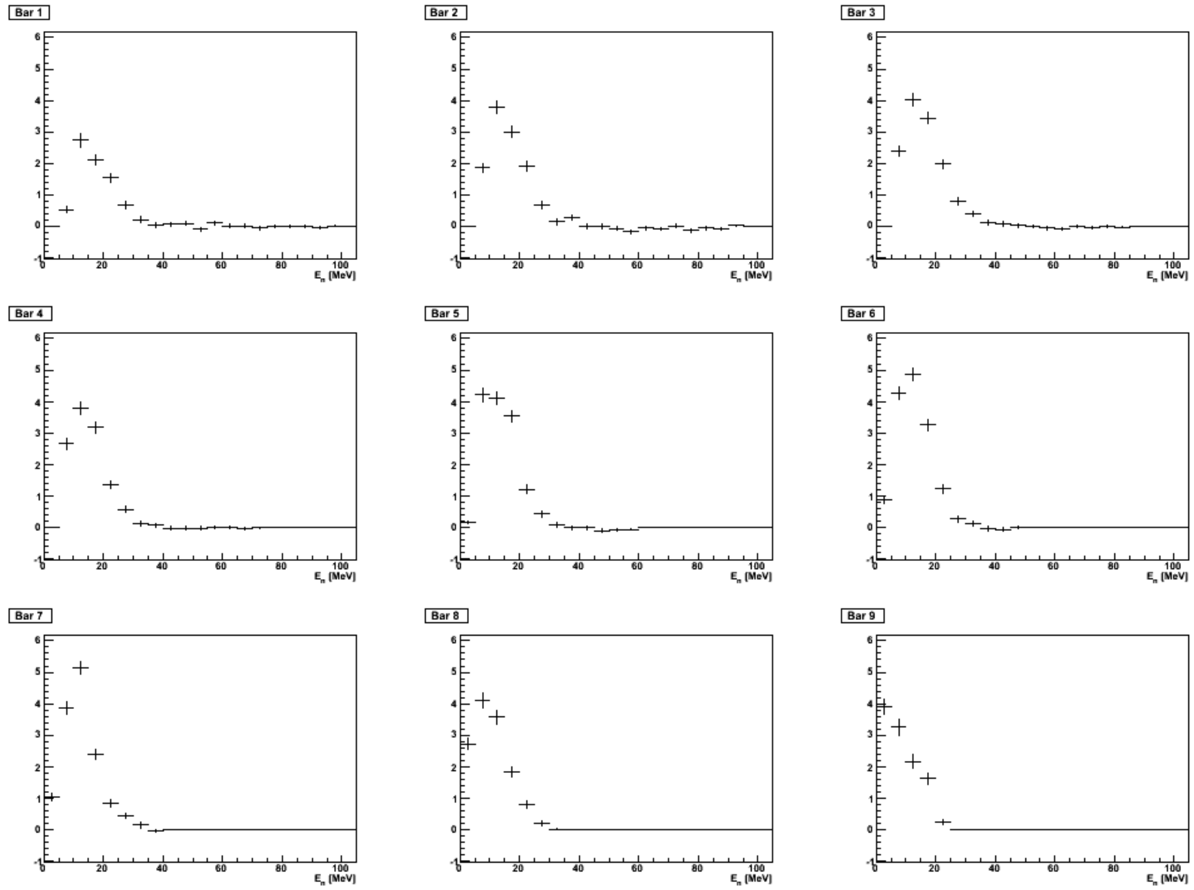

Figure 6-8: Triple differential cross section with respect to θ_p, θ_n, and E_n in units of mb/MeV/sr^2 for $E_{in} = 100 \pm 10$ MeV.

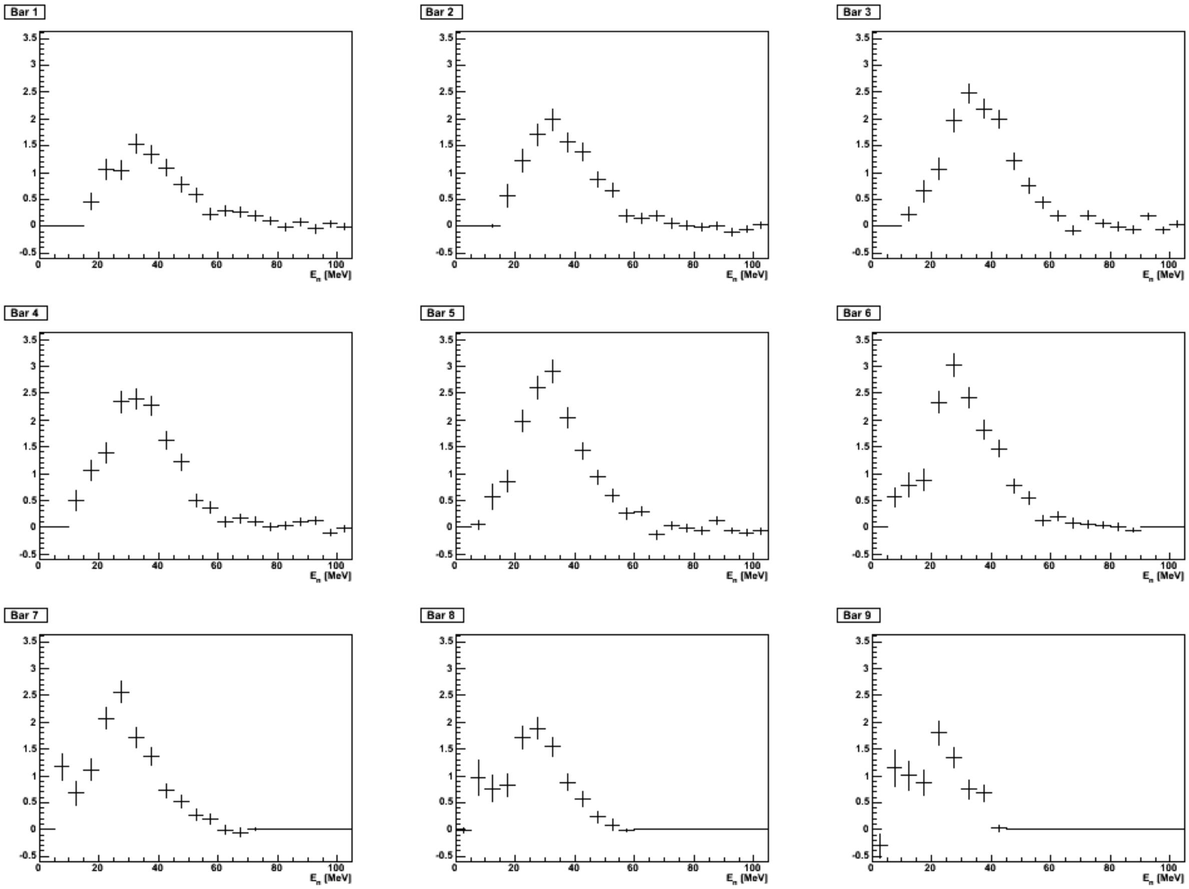

Figure 6-9: Triple differential cross section with respect to θ_p, θ_n, and E_n in units of mb/MeV/sr^2 for $E_{in} = 100 \pm 10$ MeV.

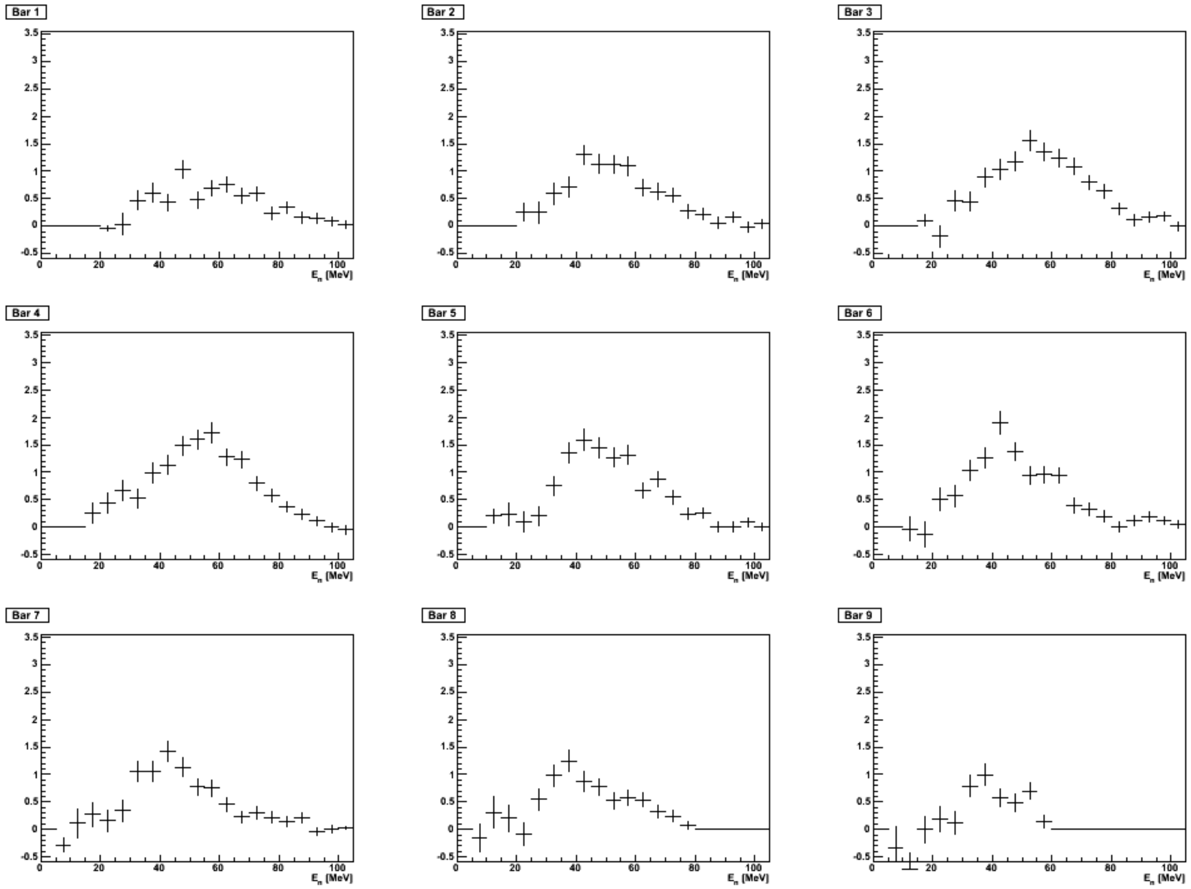

Figure 6-10: Triple differential cross section with respect to θ_p, θ_n, and E_n in units of mb/MeV/sr^2 for $E_{in} = 100 \pm 10$ MeV.

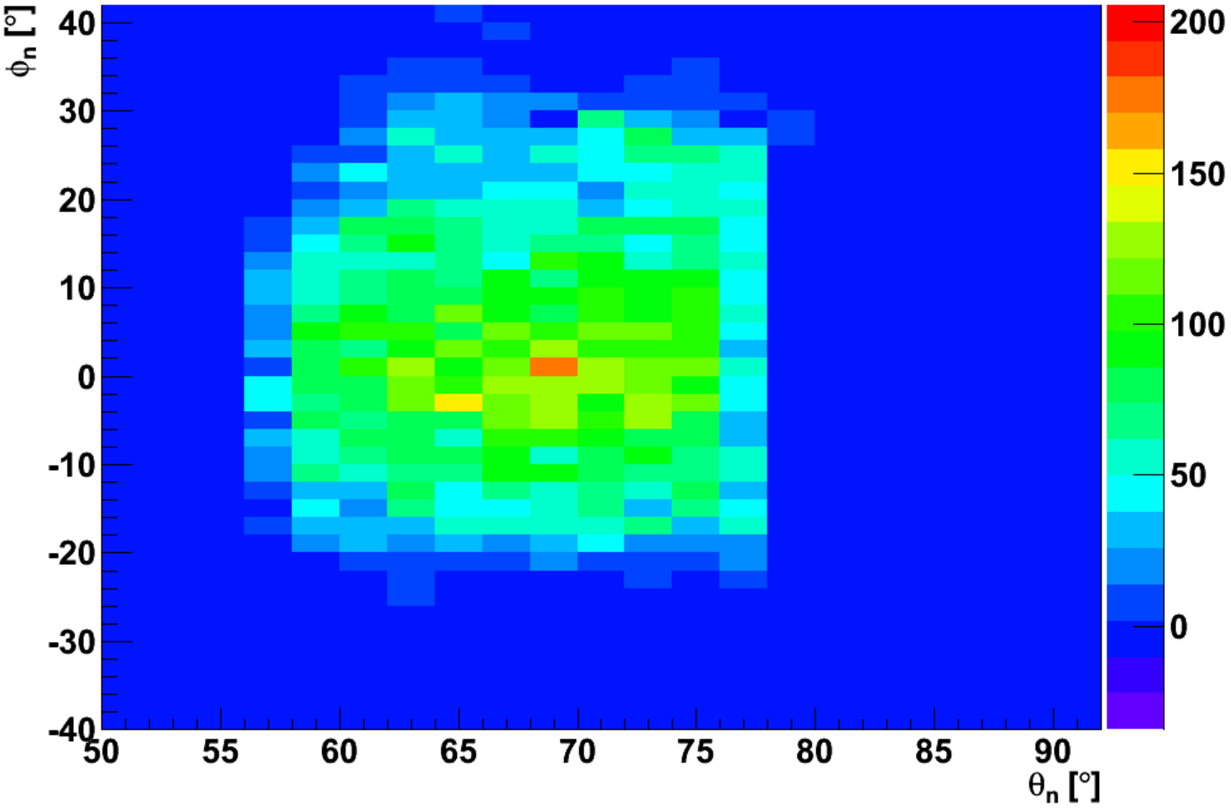

Figure 6-11: Double differential cross section with respect to θ_p and θ_n in units of mb/sr^2 for $E_{in} = 100 \pm 10$ MeV.

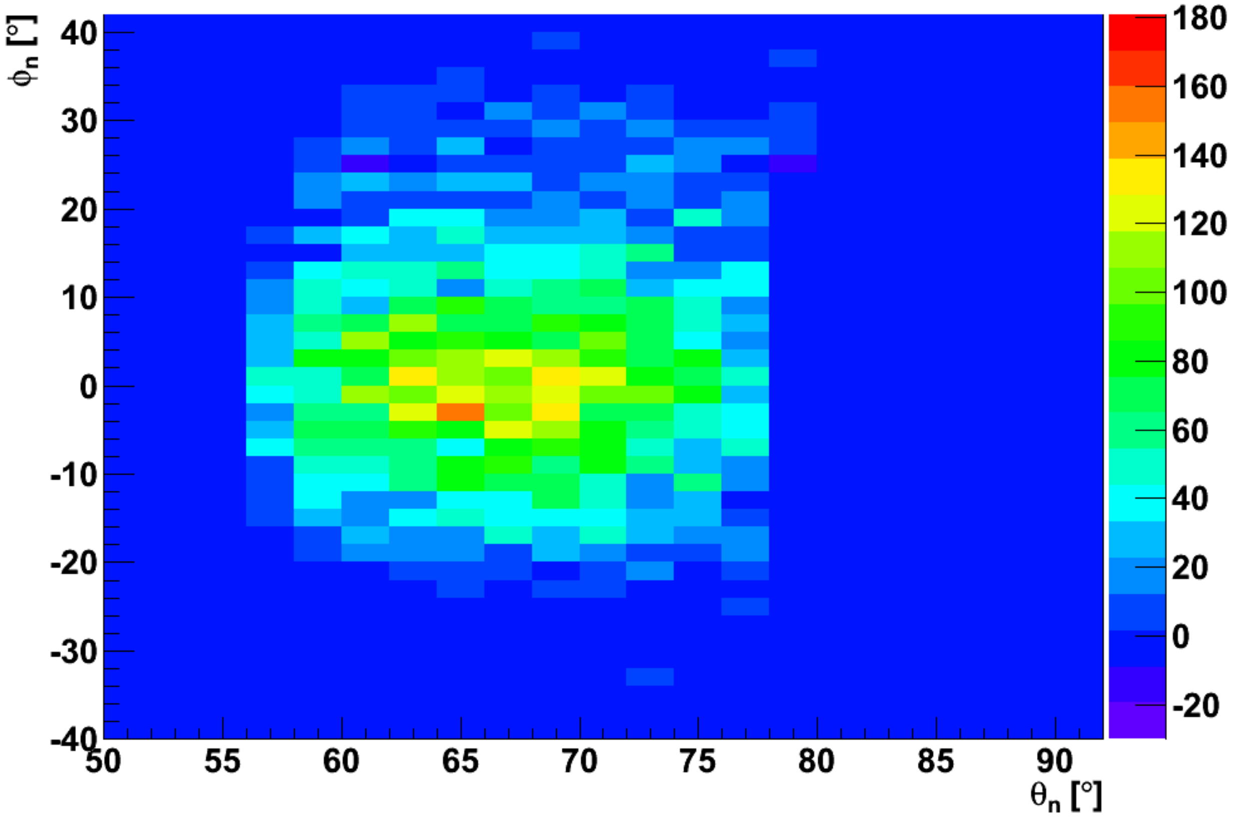

Figure 6-12: Double differential cross section with respect to θ_p and θ_n in units of mb/sr^2 for $E_{in} = 200 \pm 10$ MeV.

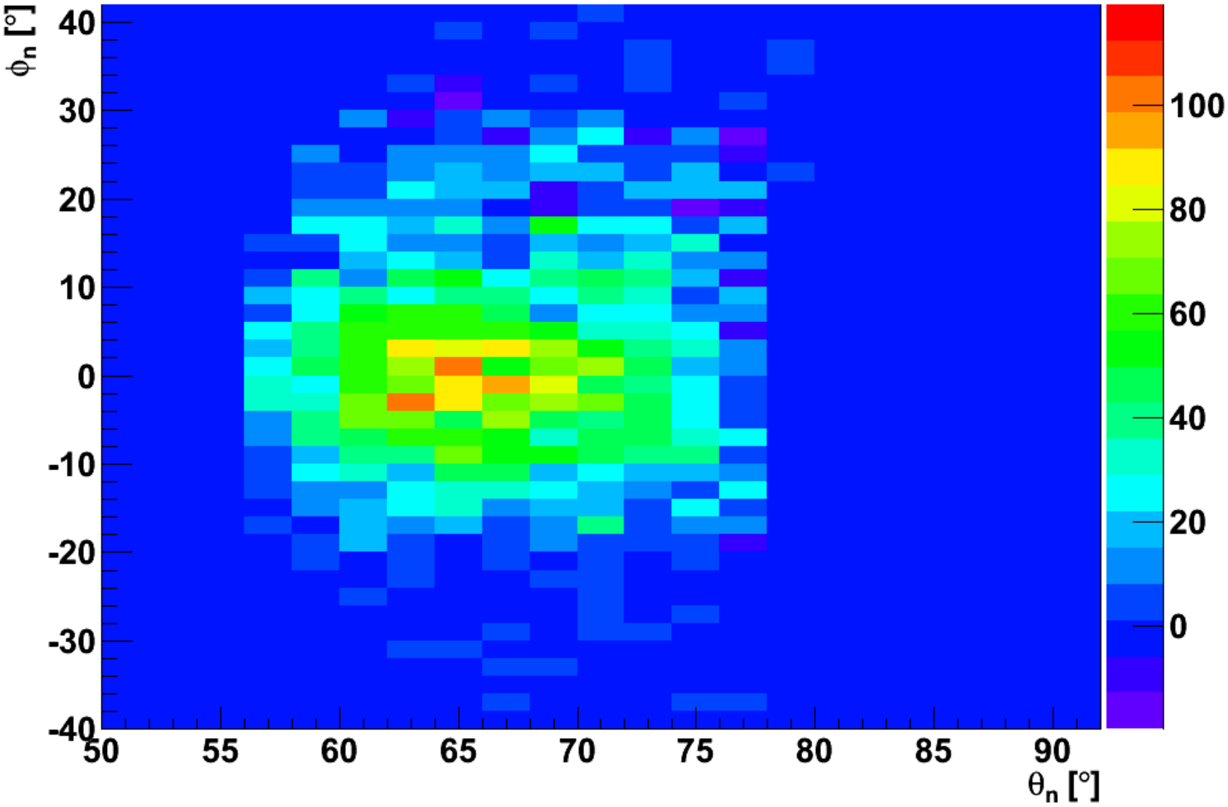

Figure 6-13: Double differential cross section with respect to θ_p and θ_n in units of mb/sr^2 for $E_{in} = 300 \pm 10$ MeV.

Chapter 7

Conclusions

This experiment successfully observed the $d(n, np)$ reaction; observed scattering angles and energies are consistent with properties of quasielastic scattering.

There are various approximations and estimates used in this analysis, which would need to be refined for a final result.

First, the neutron bar efficiencies are imprecise. This is both because no ADC thresholds were set, and because no correction was made for non-normal incidence. Both of these corrections could be made; we have cosmic and PuBe data that can be used to set ADC thresholds on the data, and the effect of non-normal incidence could be measured by simulation.

Also, the electronics dead time and target thickness values need to be measured; the dead time has not been measured, and the target thickness we used is definitely an overestimate. Analyzing the data taken with the liquid hydrogen target, for which the interaction cross section is known, would be a good way to check the various constant factors in the cross-section calculation.

Bibliography

[1] L.G. Atencio, J.F. Amann, R.L. Boudrie, and C.L. Morris. Delay-line readout drift chambers. *Nuclear Instruments and Methods in Physics Research*, 187(2-3):381–386, August 1981.

[2] M. Bernheim, A. Bussire, J. Mougey, D. Royer, D. Tarnowski, S. Turck-Chieze, S. Frullani, G. P. Capitani, E. De Sanctis, and E. Jans. Momentum distribution of nucleons in the deuteron from the d(e, e'p)n reaction. *Nuclear Physics A*, 365(3):349–370, August 1981.

[3] Kimberly K Boddy. *Charged-particle tracking for neutron-deuteron breakup*. Thesis, Massachusetts Institute of Technology, 2007. Thesis (S.B.)–Massachusetts Institute of Technology, Dept. of Physics, 2007.

[4] A. Breskin, G. Charpak, B. Gabioud, F. Sauli, N. Trautner, W. Duinker, and G. Schultz. Further results on the operation of high-accuracy drift chambers. *Nuclear Instruments and Methods*, 119:9–28, July 1974.

[5] David Brown. Low-noise amplifier for resolving the right-left ambiguity in drift chambers. *Nuclear Instruments and Methods in Physics Research Section A: Accelerators, Spectrometers, Detectors and Associated Equipment*, 226(2-3):405–410, October 1984.

[6] Maxim B. Chtangeev. *Neutron-deuteron elastic scattering and three-nucleon force*. Thesis, Massachusetts Institute of Technology, 2005. Thesis (S.M.)–Massachusetts Institute of Technology, Dept. of Physics, 2005.

[7] Taylan Akdoğan. *Pion production in the neutron-proton interaction*. Thesis, Massachusetts Institute of Technology, 2003. Thesis (Ph. D.)–Massachusetts Institute of Technology, Dept. of Physics, 2003.

[8] P. W. Lisowski, C. D. Bowman, G. J. Russell, and S. A. Wender. The Los Alamos National Laboratory spallation neutron sources. *Nuclear Science and Engineering*, 106(2):208–218, 1990.

[9] Paul W. Lisowski and Kurt F. Schoenberg. The Los Alamos Neutron Science Center. *Nuclear Instruments and Methods in Physics Research Section A: Accelerators, Spectrometers, Detectors and Associated Equipment*, 562(2):910–914, June 2006.

[10] Alice Elisabeth Ohlson. *Neutron-deuteron breakup and quasielastic scattering.* Thesis, Massachusetts Institute of Technology, 2009. Thesis (S.B.)–Massachusetts Institute of Technology, Dept. of Physics, 2009.

[11] W. Pairsuwan, J. W. Watson, M. Ahmad, N. S. Chant, B. S. Flanders, R. Madey, P. J. Pella, and P. G. Roos. Analyzing powers for the H2(p–>,pn)1H reaction at 200 MeV. *Physical Review C*, 52(5):2552, November 1995.

[12] Stefan Ritt. MIDAS home page. https://midas.psi.ch/.

[13] Jared T Turkewitz. *A Measurement of the Effective Thickness of a Liquid Deuterium Target for a Quasielastic Scattering Experiment.* Thesis, Massachusetts Institute of Technology, 2010. Thesis (S.B.)–Massachusetts Institute of Technology, Dept. of Physics, 2010.

[14] S.A. Wender, S. Balestrini, A. Brown, R.C. Haight, C.M. Laymon, T.M. Lee, P.W. Lisowski, W. McCorkle, R.O. Nelson, W. Parker, and N.W. Hill. A fission ionization detector for neutron flux measurements at a spallation source. *Nuclear Instruments and Methods in Physics Research Section A: Accelerators, Spectrometers, Detectors and Associated Equipment*, 336(1-2):226 – 231, 1993.